Fracture Process Zone Development and Length Assessment under the Mixed-mode I/II Load Analysed by Digital Image Correlation Technique

Authors Names and Affiliations

Petr Miarka[a,b*], Alejandro S. Cruces[c], Pablo Lopez-Crespo[c], Wouter De Corte[d]

[a]Institute of Physics of Materials, Czech Academy of Science, Žižkova 22, 616 00 Brno, Czech Republic

[b]Brno University of Technology, Faculty of Civil Engineering, Veveří 331/95, 602 00 Brno, Czech Republic

[c]Department of Civil and Materials Engineering, University of Malaga, C/Dr Ortiz Ramos s/n, 29071 Malaga, Spain

[d]Ghent University, Faculty of Engineering and Architecture, Department of Structural Engineering and Building Materials, Valentin Vaerwyckweg 1, 9000 Ghent, Belgium.

*Corresponding Author

Petr Miarka (email: petr.miarka@vut.cz). Tel: +420 532 290 430

Abstract

In this paper, the fracture process zone (FPZ) of high-performance concrete (HPC) is investigated under mixed-mode I/II load conditions, and its formation is studied by applying digital image correlation (DIC). The experimental tests are performed on Brazilian disc specimens with central notch (BDCN). The traction-free crack and the FPZ extent ahead of the crack are localised. This is done by modification of the existing methodology for mode I cracks to account for various mixed-mode I/II loading conditions. Analytical and linear elastic fracture mechanics (LEFM) methods for the critical strain are used to find the FPZ extension. Lastly, this paper revisits the analytical formulas used in the prediction of mode I FPZ lengths. These formulas are adjusted to allow for the prediction of the FPZ length in the whole range of mixed-mode I/II load conditions. Experimental results show that the FPZ has a different size for various mixed-mode I/II load conditions.

Keywords: HPC; FPZ; Mixed-mode I/II; DIC.

Abbreviations/Nomenclature

3PB	three-point bending
AE	acoustic emission
BDCN	Brazilian disc with central notch
CTOD	crack tip opening displacement
CTSD	crack tip sliding displacement
CS	coordinate system
DIC	digital image correlation
EA3PB	eccentric asymmetric three-point bending
EMTSN	extended maximum tangential strain
FEM	finite element method
FOV	field of view
FPZ	fracture process zone
GBFS	granulated blast furnace slag
GMTS	generalised maximum tangential stress
HPC	high-performance concrete
LEFM	linear elastic fracture mechanics
MTS	maximum tangential stress
ROI	region of interest
SC3PB	semi-circular three-point bending
SIF	stress intensity factor
WE	Williams' expansion
α	notch inclination angle (°)
ν	Poisson's ratio (-)
σ	stress (MPa)
γ	transformation angle (°)
$\sigma_{\theta\theta}$	tangential stress (MPa)
θ_0	crack initiation direction (°)
σ_t	tensile strength (MPa)

a	crack length (mm)
a/R	relative crack length (-)
B	specimen’s thickness (mm)
$C(y)$	horizontal displacement difference function (mm)
D	specimen’s diameter (mm)
d_{agg}	maximum aggregate size (mm)
E	Young’s modulus of elasticity (GPa)
f_{c}	compressive strength (MPa)
f_{ct}	flexural strength (MPa)
f_{t}	indirect tensile strength (MPa)
K_{I}	mode I stress intensity factor (MPam$^{1/2}$)
K_{IC}	mode I fracture toughness (MPam$^{1/2}$)
K_{II}	mode II stress intensity factor (MPam$^{1/2}$)
K_{IIC}	mode II fracture toughness (MPam$^{1/2}$)

l_{FPZ}	length of the FPZ (mm)
P	applied force (kN)
R	specimen’s radius (mm)
r,θ	polar coordinates (mm; °)
r_{C}	critical distance (mm)
t	notch width (mm)
T	T-stress (MPa)
u, v	displacement field in global coordinates (mm)
u_1, v_1	displacement field in local coordinates (mm)
X, Y	global coordinate system
X_1, Y_1	local coordinate system
Y_{I}, Y_{II}	shape function (-)
$\varepsilon_{\theta\theta}$	tangential strain (-)
$\varepsilon_{\theta\theta,\mathrm{C}}$	critical tangential strain (-)

1. Introduction

Concrete cracking is a complex mechanism, which is highly affected by its internal structure consisting of matrix/cement paste, aggregates and pores. Generally, the concrete cracking process involves debonding between aggregate and cement paste, crack branching into the matrix, microcracking in the matrix, and aggregate bridging of microcracks [1]. The bond between aggregate and cement paste does not represent an ideal connection and often fails in tension or shear due to its low tensile strength. The concrete’s main disadvantage is its low tensile strength, while its biggest advantage is its relatively high compressive strength. Even then, the compressive failure is associated with indirect tensile load actions [2]. Such a material behaviour has important practical consequences.

The aforementioned cracking phases occur ahead of the notch in the so-called fracture process zone (FPZ) [3]. The development of the FPZ ahead of notch/crack tip is the main reason for the quasi-brittle behaviour after reaching the peak load [4–7]. Typical properties of the FPZ to be studied are its length l_{FPZ} and width w. Both parameters can be studied by various experimental methods e.g. by acoustic emission (AE) [8,9], by X-ray computed tomography [9–12], by Moiré interferometry [13,14] and by digital image correlation (DIC) [15,16] or by combination of DIC and AE [17–20].

The FPZ is normally investigated on various specimen geometries and test setups. Most of them use a prismatic three-point bending (3PB) test configuration [16,21], or wedge-slitting test (WST) configuration [22] to investigate the FPZ under the tensile mode I. This was recently extended by the use of a semi-circular three-point bending (SC3PB) [23,24] test configuration.

Contrary to this, structural applications do not often exhibit a pure mode I crack opening loading. The loads present on structures are often a combination of tensile and shear mode loading, i.e. mixed mode I/II. The mixed-mode I/II loading is a result of the structural behaviour or construction technology. A typical example of a mixed-mode I/II structural failure is found in simply supported reinforced beam with steel stirrups [25–27] and pre-tensioned precast hollow floor panels [28,29] which can both fail due to compressive failure of the diagonal. Other mixed-mode I/II failure mechanisms can be observed for cast-in anchors [30].

The mixed-mode I/II fracture is investigated for almost six decades [31,32] and it goes hand in hand with the progress of linear elastic fracture mechanics (LEFM). Due to presence of mixed-mode I/II loading, the crack starts to kink from a straight path, when the load increases. This phenomenon has been studied for both static and fatigue cracks of metallic materials [33]. Such studies have led to the formulation of mixed-mode I/II fracture criteria, which are able to predict such failure. The basic criteria used for the mixed-mode I/II fracture assessment are the maximum tangential stress (MTS) [34] and the strain energy density (SED) [35]. In addition, the mixed-mode I/II load conditions affect the FPZ in the concrete in a similar manner as it affects the crack path in metallic alloys [36,37]. The crack as well as FPZ deflection are schematically shown under different mixed-mode I/II conditions in Figure 1.

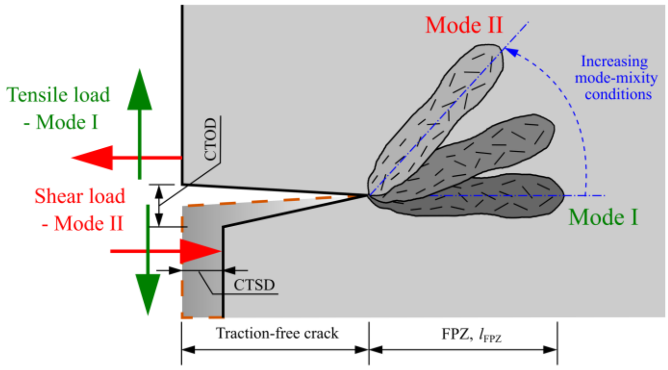

Figure 1: Influence of mode-mixity on the shape of FPZ.

The FPZ deflects from the straight path due to presence of mixed-mode I/II and increasing mode II loading is shown in Figure 1. Such behaviour of a FPZ was recently studied by Lin et. al. [38] using the eccentric asymmetric three-point bending (EA3PB) test with rectangular cross-section. This study showed that the mixed-mode I/II loading not only deflects the FPZ from vertical the direction but it also increases its length due to crack face sliding. This was documented by measurement of the crack tip opening (CTOD) and crack tip sliding (CTSD) displacements as shown in Figure 1. Increased CTSD, i.e. mode II deformation, eventually results in a lower load capacity by approx. 15 %, if compared with the maximum load of mode I specimens. The measured values of CTOD and CSTD could be used in a vector mixed-mode I/II criterion [39,40] to determine the crack initiation direction.

Recently, the mixed-mode I/II load conditions were studied using an SC3PB test with inclined notch [41] and by using Brazilian disc specimens with central notch (BDCN) [42,43]. Researchers have enriched these studies by making use of DIC, e.g. to obtain values of the Williams' expansion (WE) [44] terms, verify the accuracy of analytical and finite element method (FEM) numerical solutions (See [45–47]) and using the *J*-integral to calculate the fracture toughness [48]. The biggest advantage to use a BDCN specimen in material testing, lies in the testing of renovated concrete structures prior to renovation as they are usually analysed by core-drill samples to obtain basic information about the material performance. This immediately allows to obtain the material's fracture parameters without reshaping into a prismatic specimen with rectangular cross-section. The derived fracture parameters serve then as an input to the advanced material models as implemented in commercial FEM software [49–52]. Thus, the improved structural design often leads to the reduction of material consumption as well as to extension of the structure's service lifetime.

The experimental study in this paper focuses on the analysis of the FPZ development under various mixed-mode I/II loading conditions this time studied on BDCN specimens. For this, DIC displacements and strains were captured during the test. The main interest was placed on the area close to the initial notch located at the centre of disc with an intent to comprehensively describe the development and finite size of the FPZ under mixed mode I/II load conditions. In addition to this, we propose adjustments to the traction-free crack localisation methodology and the assessment of the extent of the FPZ based on LEFM assumptions. The experimentally observed size and shape of FPZ were supported by measurement of the CTOD and the CTSD vector components. The last part of the paper revisits the traditional analytical formulas used in the FPZ length prediction. The mentioned experimental results again support the proposed changes to account for the mixed-mode I/II loading with relatively good agreement.

2. Theoretical Background

In this theoretical background, we begin with a brief description of the stress field in a cracked body under mixed-mode I/II load conditions based on the well-acknowledged Williams' expansion (WE). We then present the description of the tangential strain component $\varepsilon_{\theta\theta}$ and its application to mixed-mode I/II fracture assessment. Finally, we present the Brazilian disc with central notch (BDCN) together with analytical formulas to obtain values of stress intensity factors (SIF). This provides a solid base for the analysis of the size and shape of the fracture process zone in concrete under mixed-mode I/II load conditions.

2.1 Mixed-mode I/II

The Williams's expansion (WE) [44] uses LEFM for the description of the stress and displacement fields in a cracked body. The WE is an infinite power series in which the number of terms influences the accuracy and precision of the calculated stresses and displacements [53,54]. The first terms are related to *K*/SIFs for both mode I and mode II load conditions and the first non-singular term is related to the *T*-stress. Additionally, the *T*-stress is related to mode I crack opening and is independent on the distance from the crack tip. Using these two parameters of the WE, the stress field in a cracked body can be described as follows:

$$\sigma_{i,j} = \frac{K_I}{\sqrt{2\pi r}} f_{i,j}(\theta) + \frac{K_{II}}{\sqrt{2\pi r}} g_{i,j}(\theta) + T + O_{i,j}(r,\theta), \tag{1}$$

where σ_{ij} represents the stress tensor components, K_I, K_{II} are the mode I and mode II SIFs, $f_{i,j}(\theta)$ and $g_{i,j}(\theta)$, are known shape functions for mode I and mode II, T (or T-stress) is the first non-singular term independent from the distance r, O_{ij} are the higher order terms and r, θ are the polar coordinates (with origin at the crack tip; the crack faces lie along the X-axis and the coordinate system rotates with any new crack increment or rotation).

Similarly to stress components, the strain components can be calculated using the WE. Since this study set its main goal to describe the FPZ by DIC experimental data, using strains for the analysis of a cracked body seems more logical as strains are one of the primary DIC outputs. Strains calculated by the WE take into account material properties E – Young's modulus of elasticity and ν – Poisson's ratio. This leads to a more accurate crack analysis as the stresses in the WE use $\nu = 0$ and are considered to act under plane strain conditions, while on the surface this is not valid [55]. The stress tensor components are shown in Figure 2(a), while the strain components are presented in Figure 2(b).

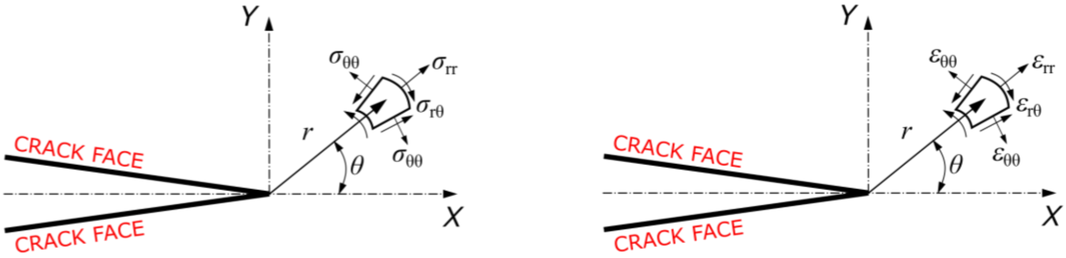

(a) (b)

Figure 2: Stress (a) and strain (b) components in front of a crack in a polar coordinate system.

As can be seen in Figure 2(a) and Figure 2(b), the crack opening component is in the tangential ($\theta\theta$) direction for any mode I and mode II load combination. Thus, the tangential strain $\varepsilon_{\theta\theta}$ will be used in further analysis and can be calculated as:

$$\varepsilon_{\theta\theta} = \frac{1}{E}(\sigma_{\theta\theta} - \nu\sigma_{rr}), \tag{2}$$

where E is the Young's modulus of elasticity, ν is the Poisson's ratio and $\sigma_{\theta\theta}$ and σ_{rr} are the tangential and radial components of the stress tensor in polar coordinates, respectively.

The tangential strain $\varepsilon_{\theta\theta}$, as shown in Eq. (2), can be described by using the WE:

$$\varepsilon_{\theta\theta} = \frac{K_I}{E\sqrt{2\pi r}}(f_{\theta\theta} - \nu f_{rr}) + \frac{K_{II}}{E\sqrt{2\pi r}}(g_{\theta\theta} - \nu g_{rr}) + \frac{T}{E}(sin^2\theta - \nu cos^2\theta), \tag{3}$$

where $f_{\theta\theta}$, f_{rr}, $g_{\theta\theta}$ and g_{rr} are the known geometry functions of angle θ for mode I and mode II. All these functions are presented in more detail in Appendix A – Williams' Expansion Functions.

Eq. (3) can be used in the extended maximum tangential strain (EMTSN) criterion as formulated by Mirsayar [56,57]. The EMTSN criterion is a derivation from the traditional Erdogan MTS criterion [34] which uses both SIFs and *T*-stress in the assessment of the material's fracture. In addition to this criterion, literature offers additional two-parameter criteria e.g., the generalised maximum tangential stress (GMTS) criterion [58] or the generalised strain energy density (GSED) criterion [59]. The GMTS found application in rocks [60], in concrete in [61–63], as well as in mortar [64].

Moreover, these fracture criteria relate damage of the specimen to the mode I fracture toughness K_{IC} and usually plot results in relative coordinates K_I/K_{IC} and K_{II}/K_{IC}. Generally, such plots show relatively good results for the experimental data with a dominant mode I load. With increasing mode II dominance, the scatter increases from the curve predicted by one of the selected criteria (see [61,62]). Some studies [56,58] overcome this setback by using the effective value of SIF K_{eff} as a geometric sum of both types of SIFs as:

$$K_{eff} = \sqrt{K_I^2 + K_{II}^2}. \tag{4}$$

2.2 Brazilian Disc with Central Notch (BDCN)

A BDCN specimen was selected in this study due to the relatively simple specimen preparation and experimental testing, but mainly due to presence of mixed mode I/II loading. Since the BDCN specimen has its notch placed in the centre of the disc, an independent analysis of both notch tips can be performed. This doubles the information obtained during the experimental test, if compared with a standard 3PB or SC3PB test specimen. The BDCN specimen [65], its cross-section and boundary conditions are shown in Figure 3.

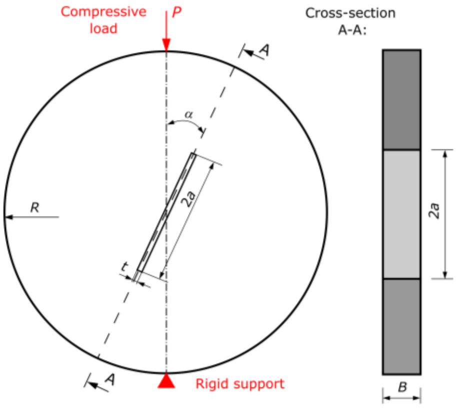

Figure 3: Dimensions, cross-section, and boundary conditions of a Brazilian disc with central notch (BDCN).

The mixed-mode I/II loading is achieved by inclining the initial notch to the loading point at an angle α. Then, the SIF values for each crack opening mode are calculated using Eq. (5):

$$K_i = \frac{P\sqrt{a}}{RB\sqrt{\pi}} \frac{1}{\sqrt{1-\frac{a}{R}}} Y_i(a/R,\alpha), \tag{5}$$

where *i* is the crack opening mode I or II, *P* is the applied compressive load, *R* is the specimen radius, *a* is the crack length, α is the notch inclination angle, *B* is the thickness of the specimen and Y_i are the shape functions for mode I and mode II, respectively.

The values of the shape functions for mode I and mode II can be found in literature, e.g. in the handbook by Tada & Paris [66] or in papers by Ayatollahi & Aliha [60], Seitl et al. [61] and Fett [67]. Similarly to values of SIFs, solutions of the elastic *T*-stress can be found in works by Leevers & Radon [68] and Fett [67]. Both shape functions Y_i are shown in Figure 4(a) for relative notch length of 0.26 and 0.4.

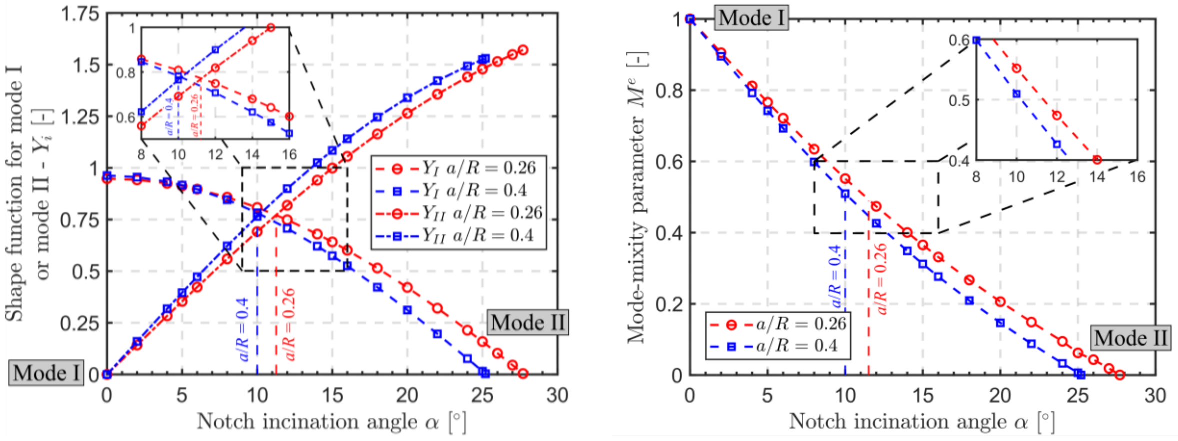

(a) (b)

Figure 4: Comparison of the differences between the geometry shape functions Y_i (a) and (b) - Mode-mixity parameter M^e for various relative notch lengths *a*/*R*.

In this study, two different notch lengths *a*/*R* are chosen, due to the different mode-mixities present ahead of the crack tip. As can be observed from Figure 4(a), values of shape functions Y_i indicate equal values for mode I and mode II at angles α for different *a*/*R* ratios. The values of shape function for mode I and mode II are equal for α = 11.5° for *a*/*R* = 0.26, while for *a*/*R* = 0.4 this occurs for an angle α = 10°. This, if studied experimentally, provides useful information about the material's cracking process.

Relying only on the values of shape functions Y_i can be misleading as the inner stress conditions of BDCN will vary according to the values of the SIF, which considers the real geometry of the specimen. These stress conditions are often described as a mode-mixity ratio usually expressed by the parameter M^e (see [69]) as:

$$M^e = \frac{2}{\pi} arctan\left(\frac{K_I}{K_{II}}\right), \tag{6}$$

The parameter M^e varies from zero (for pure mode II) to one (for pure mode I). The development of the mode-mixity parameter M^e for various notch inclination angles α and for both studied notch lengths *a*/*R* is shown in Figure 4(b).

In Figure 4(b), a small difference in the values of mode-mixity parameter M^e for relative notch ratios *a*/*R* = 0.26 and 0.4 can be seen, especially for the angles α for which mode I should be equal to mode II (10° and 11.5°). However, this marginal difference observed for parameter M^e has a small influence on the stress conditions ahead of the crack tip and consequently on crack initiation and propagation. Additionally, the Figure 4(b) indicates a higher mode I dominance for a ratio *a*/*R* = 0.26 when compared to *a*/*R* = 0.4, which was not observed in Figure 4(a) for geometry shape functions Y_i.

Since the BDCN specimen offers the possibility to test the material in the whole range of the mixed-mode I/II we propose adjustment to the effective SIF as presented in Eq. (4). This proposed adjustment is based on a unit circle in a coordinate system Y_{I}-Y_{II} (the reader is referred to Appendix B – Effective Fracture Toughness for more details). The proposed adjustment of the shape functions of Eq. (4) has the following form:

$$Y_{EFF} = \sqrt{\left(Y_{I,\alpha_I} \cos\left(\frac{90°}{\alpha_{II}}\alpha\right)\right)^2 + \left(Y_{II,\alpha_{II}} \sin\left(\frac{90°}{\alpha_{II}}\alpha\right)\right)^2}, \qquad (7)$$

where α_{II} is the notch inclination angle for pure mode II loading, Y_{I,α_I} is the value of the shape function for pure mode I and $Y_{II,\alpha_{II}}$ is the value of the shape function for pure mode II. Using Eq. (7) one can obtain the effective value of the shape function based on the notch inclination angle α for various relative notch lengths a/R. To demonstrate a valuable practical implication of Eq. (7), an effective shape function Y_{EFF} is plotted together with the values of Y_{I} and Y_{II} in Figure 5 for both analysed a/R ratios.

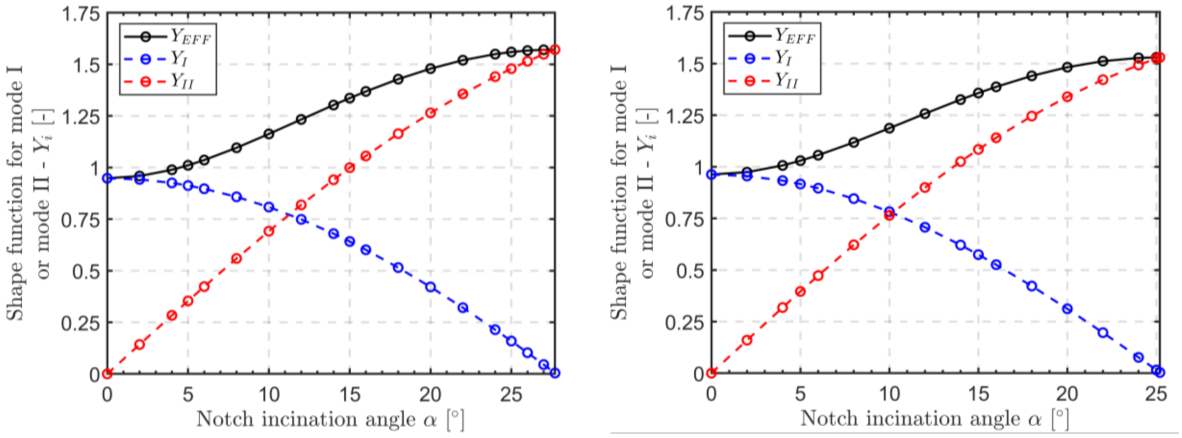

(a) (b)

Figure 5: Comparison of effective shape function Y_{EFF} for two a/R ratios (a) – a/R = 0.267 and (b) – a/R = 0.4.

Figure 5(a) and Figure 5(b) show values of the effective shape function Y_{EFF} for all notch inclination angles α. This can be used in the whole range of the mixed-mode I/II fracture assessment and simultaneously, it can be used for simple mode I and mode II fracture analysis.

3. Materials and Methods

In what follows, the concrete mixture together with its mechanical properties and the specimen dimension are introduced. Afterwards, we show the proposed changes to evaluate the fracture toughness, which can be employed in the whole range of mixed-mode I/II load conditions. Then, we briefly present experimental technique to capture the displacement digital image correlation (DIC). Finally, we present the method for crack tip acquisition under mode I and mixed mode I/II loading conditions.

3.1 Mixture Composition

The studied HPC mixture was designed with the intent to produce lighter precast concrete elements and reduce the cement consumption. For this, Portland cement CEM I 42.5 R was combined with three mineral admixtures, see [70]. The binder was blended in a ratio of 81 % CEM I 42.5 R, 9.5 % metakaolin, 7.5 % granulated blast furnace slag (GBFS) and 2.5 % limestone. To achieve good workability, a polycarboxylate-based superplasticizer (Glenium 300) was used due to the low water/binder ratio of 0.22. The aggregates consist of natural sand 0/4 mm and crushed high quality granite 4/8 mm. The mixture was mixed in a small volume batches of 0.7 m^3 and poured directly into moulds. The material composition per m^3 is shown in Table 1.

Table 1: Material composition of the studied HPC per m^3.

	CEM I 42.5R	GBFS	Limestone	Metakaolin (Metaver)	Superplasticizer (Glenium 300)	Water	Sand 0/4	Crushed aggregates 4/8
[kg]	650	60	15	75	17	165	400	600

Prepared samples were covered with a PE-foil to prevent excessive moisture exchange with the environment due to storing the specimens outside of the laboratory environment (i.e., at precast concrete plant), with a changing temperature ≈ 5 - 25°C for a period of 28 days. Afterwards, at the age of 28 days, the mechanical properties of this HPC mixture were measured in accordance with European standards and are presented in Table 2.

Table 2: Mechanical parameters (mean values with their standard deviations) of the studied HPC at 28 days.

Compressive strength $f_{\mathrm{c,cube}}$ [MPa]	106.2 ± 2.5
Young's modulus E [GPa]	41.0 ± 0.6
Flexural strength $f_{\mathrm{c,t}}$ [MPa]	9.3 ± 0.9
Indirect tensile strength f_{t} [MPa]	6.43 ± 0.3

3.2 Effective Fracture Toughness

In order to demonstrate the validity of proposed adjustment to the calculation of the effective SIF under mixed-mode I/II loading we compare previously measured fracture forces P_{C} on the same material [46,63] with the back-calculated values of the fracture force P_{C} using Eq. (5). The values of shapes function in Eq. (7) can be substituted with the values of the fracture toughness for mode I K_{IC} and for mode II K_{IIC} as:

$$K_{C,EFF} = \sqrt{\left(K_{IC}\cos\left(\frac{90°}{\alpha_{II}}\alpha\right)\right)^2 + \left(K_{IIC}\sin\left(\frac{90°}{\alpha_{II}}\alpha\right)\right)^2}, \tag{8}$$

where $K_{\mathrm{C,EFF}}$ is the effective fracture toughness dependent on the notch inclination angle α and α_{II} is the notch inclination angle for pure mode II.

To begin this demonstration, we show previously measured [46,63] values of fracture toughness for mode I and mode II on the same material. In addition to this, mean values for each mode are shown to illustrate differences between the mode I K_{IC} and the mode II fracture toughness K_{IIC}. These values are presented in Table 3.

Table 3: Comparison of measured values of fracture toughness for mode I and mode II.

Mode I				Mode II			
a/R [-]	Angle α [°]	K_{IC} [MPamm$^{1/2}$]	mean K_{IC} [MPamm$^{1/2}$]	a/R [-]	Angle α [°]	K_{IIC} [MPamm$^{1/2}$]	mean K_{IIC} [MPamm$^{1/2}$]
0.26	0	33.5	33.76	0.26	27.7	50.05	53.01
	0	34.02			27.7	55.98	
0.4	0	38.73	36.09	0.4	25.2	48.71	51.06
	0	33.45			25.2	53.41	
Mean for both a/R K_{IC} [MPamm$^{1/2}$]		34.93		Mean for both a/R K_{IIC} [MPamm$^{1/2}$]		52.04	

In Table 3 a mean value of the fracture toughness from all data can be seen together with separated mean values for each relative notch length a/R. The difference observed for different mean values of fracture toughness is less than 5% for mode I and less than 3 % for mode II.

To back-calculate the fracture force P_{C}, Eq. (5) is used with the substitution of the SIF with the effective fracture toughness $K_{\mathrm{C,EFF}}$ obtained from Eq. (8). The geometric input to Eq. (5), the disc's radius R of 75 mm and thickness B of approx. 30.5 mm together with initial notch length $2a$ were used as mean values obtained from measured data. The comparison of the back-calculated and experimentally measured fracture forces P_C for different notch inclination angles is showed in Figure 6.

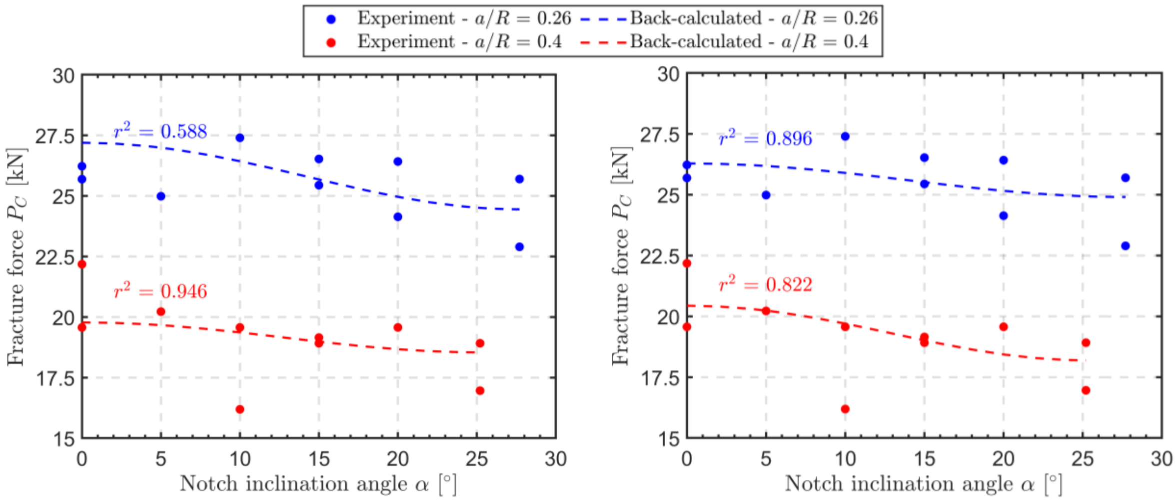

(a) (b)

Figure 6: Comparison of back-calculated and experimentally measured fracture forces P_C using – (a) average values of K_{IC} and K_{IIC} for every relative notch length a/R and (b) – average value of K_{IC} and K_{IIC} for whole data set.

The comparison presented in Figure 6(b) shows an improvement in the back-calculated fracture forces P_C, if compared to the results presented in Figure 6(a) for ratio $a/R = 0.26$. This better prediction is due to the use of mean value of fracture toughness K_{IC} and K_{IIC} for both relative notch lengths a/R ratio. This error can be reduced by using more specimens to obtain values of K_{IC} and K_{IIC}, which are the main parameter in the Eq.(8). Thus, for easier interpretation of the experimental results, in what follows, we will use a mean value obtained from all the data related to the mode I $K_{IC} = 34.93$ MPa mm$^{1/2}$ and mode II fracture toughness $K_{IIC} = 52.04$ MPa mm$^{1/2}$.

The measured fracture forces P_C for pure mode II load conditions shows lower values than the forces measured for mode I load case. This agrees with the results obtained by Lin and co-authors [38]. The results of back-calculated fracture forces P_C presented in Figure 6 show a reasonable error in whole range of a tested experimental data, which was achieved by knowing only two material's parameters (K_{IC} and K_{IIC}) and using the theoretical value of the specimen's the geometry (α_{II}) to produce pure mode II loading. Based on this, we believe that the use of the effective fracture toughness $K_{C,EFF}$ could lead to a further practical application of the BDCN test in fracture analysis of concrete under mixed-mode I/II prior to the renovation of a concrete structure.

3.3 Specimen's Geometry and Test Equipment

In this experimental study, two different notch lengths $2a$ and various notch inclination angles α were used on BDCN specimens to obtain mixed-mode I/II load. The BDCN specimens were cut to the required thickness using a diamond blade saw from a standardized cylinder. The prepared BDCN specimens from cylinders had a diameter D of approx. 150 mm (radius $R = D/2$) with a thickness B of approx. 30 mm. A straight-through notch was achieved by using a water jet cutter. The initial notch had lengths $2a$ of 40 and 60 mm, respectively.

The experimental tests were performed under mode I, mixed mode I/II and under pure mode II load conditions. The different mode-mixity conditions are achieved by varying the notch inclination angle α against the load position (please note that the angle α related to pure mode II varies based on the selected a/R ratio see Figure 4(a)).

A speckle pattern was applied on the surface of the BDCN specimens to produce a random grey intensity distribution. The size of coarse aggregates is not suitable for direct DIC data acquisition as they are larger than the used subset of pixels. This speckle pattern was obtained by spray painting the specimen's surface with black and white speckles. This allowed for a correct DIC displacements and strains acquisition.

A MTS servo-hydraulic rig was used for the static fracture tests with a maximum capacity of 100 kN. This testing rig is able to induce vertical displacement with a speed of 0.01 mm/s. A Flir Gazelle CCD camera with a resolution of 4.1 MPxl and acquisition speed of 150 FPS was used to capture pictures during the fracture test. To ensure good homogeneous light conditions for proper DIC measurements, this camera was combined with a Schneider lens coupled with two light sources. The working distance was increased to 80 cm to reduce misalignment error. Due to brittle behaviour of the test, 150 pictures were taken each second. This equipment arrangement provides a field of view (FOV) of 181.24 × 181.24 mm^2. The digital images were processed by VIC 2D V6 software in order to obtain a displacement and strain field [71]. This test set-up is based on a previous study [46]. The BDCN specimens with the speckle pattern are shown in Figure 7.

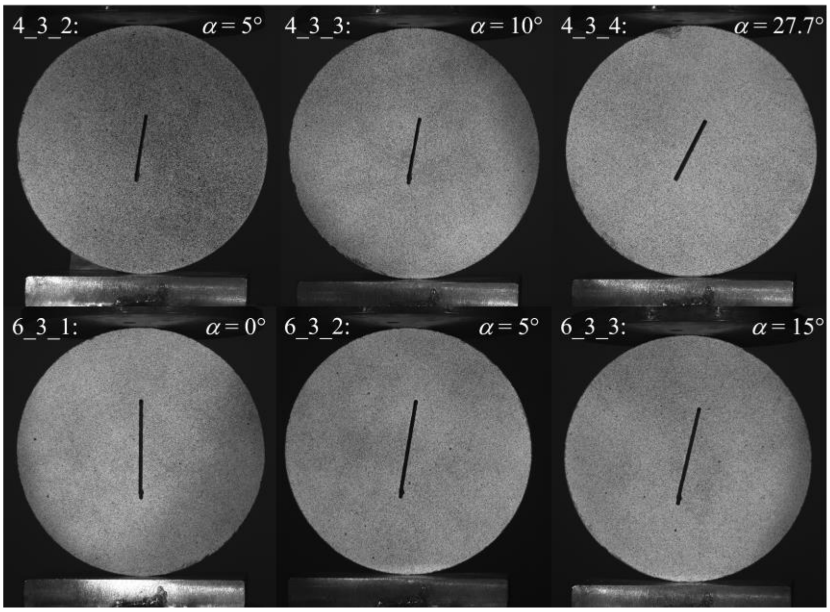

Figure 7: BDCN specimens with applied speckle pattern.

In total, six BDCN specimens were used in this experimental study. The specimen numbering refers to dimension of the initial notch lengths 2*a*, disc thickness *B* and to the number of the specimen of each *a*/*R* ratio. The measured dimensions of *D*, *B* and 2*a* of used specimens are presented in Table 4.

Table 4: Measured dimensions of the used Brazilian disc specimens.

Specimen	*a/R* [-]	*α* [°]	*D* [mm]	*B* [mm]	2*a* [mm]
4_3_2	0.271	5	149.18	30.65	40.46
4_3_3	0.269	10	149.23	30.47	40.08
4_3_4	0.271	27.7	149.21	31.50	40.41
6_3_1	0.406	0	149.18	30.56	60.59
6_3_2	0.403	5	149.23	30.48	60.21
6_3_3	0.404	15	149.17	30.56	60.29

Specimen 4_3_1 was used as a preliminary specimen to test the machine settings (loading speed) and to verify the speckle pattern for the DIC measurements.

3.4 DIC Data Extraction

DIC was used to analyse displacements and strains fields of the BDCN specimens with various crack lengths and various inclination angles *α* (mixed-mode I/II load). DIC provides full-field displacement information of the strained specimen's body [72] by comparing images taken before and after inducing load to the tested specimen. Each captured image is then splitted into smaller regions, or 'interrogation windows'. The cross-correlation product [73] is used to determine the connection between the interrogation windows before and after straining the specimen's body as:

$$c'(u,v) = \frac{\sum_{x=-\frac{N}{2}}^{y=\frac{N}{2}}\sum_{x=-\frac{N}{2}}^{y=\frac{N}{2}} I_A(x,y) I_B(x+u,y+v)}{\sqrt{\sum_{x=-\frac{N}{2}}^{y=\frac{N}{2}}\sum_{x=-\frac{N}{2}}^{y=\frac{N}{2}} I_1^2(x,y)\sum_{x=-\frac{N}{2}}^{y=\frac{N}{2}}\sum_{x=-\frac{N}{2}}^{y=\frac{N}{2}} I_2^2(x+u,y+v)}}, \tag{9}$$

where *c'* is the normalised cross-correlation product, which is a function of *u* and *v*, these being the displacement vectors joining the centres of the two regions of interest along directions *x* and *y*, respectively. I_A and I_B are the intensity distributions of the two digital images before and after straining the sample, respectively, and *N* is the number of interrogation windows into which the digital images were divided. The maximum value of the normalised cross-correlation product (Eq. (9)) is the probable displacement vector for the centre of each interrogation window in I_A. This improves the resolution of the analysis and makes post-processing easier and faster [74,75]. 29×29 pixel subsets with a 7 pixel step were used in the DIC processing, providing a 0.62mm resolution in terms of strains.

DIC requires the surface to have a random pattern so that each interrogation window is unique in each image and can be located easily in the same image after it has undergone some deformation or rigid body movement.

To detect notch tip location, a Sobel's edge-finding algorithm as implemented in the MATLAB image processing toolbox [76] was used. Sobel's algorithm is predominantly used in the image processing analysis as it searches for regions with significant discontinuities. This can be easily applied to a fracture analysis of a 2D displacement map, where the discontinuity is the crack. The algorithm assigns value of 1 to the regions/pixel with a significant discontinuity, and a value of 0 elsewhere. The found edge, in this case initial notch, is located at the region with a value of 1. The crack/notch tip is located along the border points where an edge was detected.

This approach was previously used in fatigue and fracture applications [77,78]. An interesting comparison of different methods for locating the crack tip from DIC maps [79] is also available. To the authors' knowledge, this is the first time that such a procedure has been applied to concrete.

Typical horizontal displacement fields *u* and vertical displacements *v* with marked notch tip locations are shown in Figure 8.

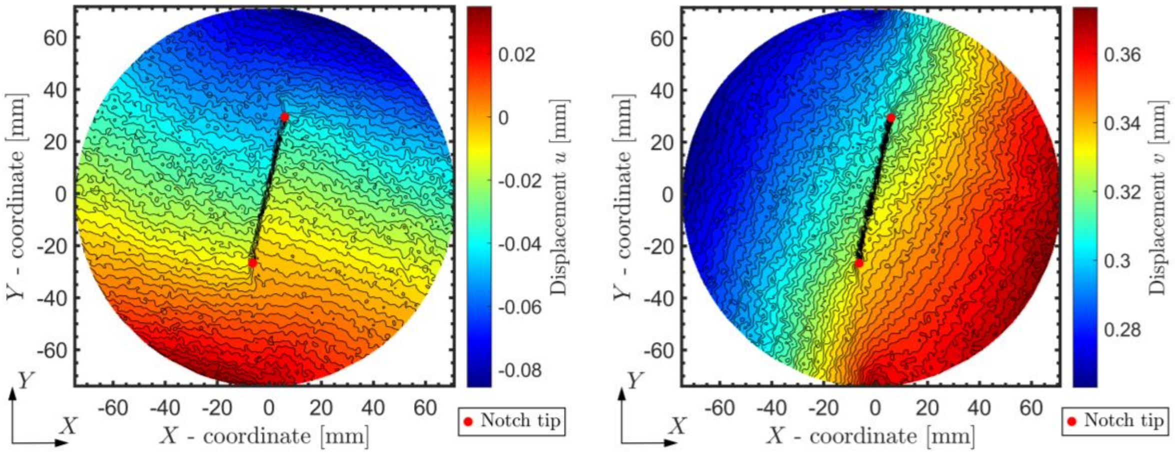

(a) (b)

Figure 8: Captured displacement fields by DIC technique of $a/R = 0.4$ and $\alpha = 5°$ with a location of the notch tips– (a) horizontal displacement *u* and (b) – vertical displacement *v*.

A slight asymmetry in both displacement fields can be observed in Figure 8. This asymmetry in displacement fields indicates the presence of a local mode II deformation in the region of notch tip. Such mode II deformation has a major influence on shape of the FPZ and on the crack initiation direction. In both Figure 8(a) and Figure 8(b) a small discontinuity generated by initiating crack can be observed. This discontinuity is running parallel to the *Y* axis towards the loading point (top edge of the disc) and towards the rigid support (bottom edge of the disc). Both discontinuities generated by notch and by crack were detected by Sobel's edge-finding routine following the strategy previously described [75].

To identify and analyse the size and shape of the FPZ under the mixed-mode I/II conditions, we reduced the region of interest (ROI) of the measured DIC data to the close location around the notch tip with a dimension of $40 \times 60\ \text{mm}^2$. The ROI was placed so it captures the bottom and top notch location, where the crack and FPZ are expected to be present. The reduced ROI marked on both notch ends is shown in Figure 9 with white dashed-line rectangles.

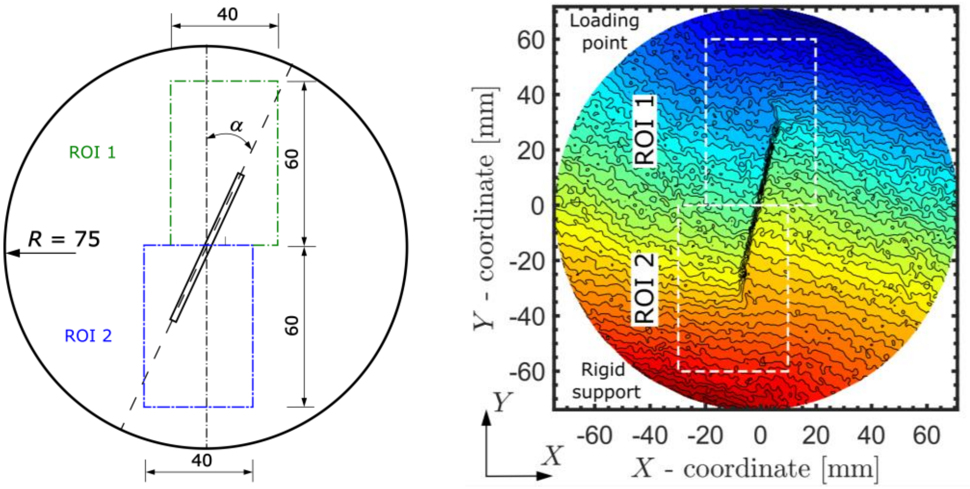

(a) (b)

Figure 9: Reduced ROI – (a) schematic location and (b) – ROI placed in horizontal displacement *u* map.

The reduced ROI as presented in Figure 9 allows for an independent analysis of each notch end, while keeping the same resolution of the data. In addition to this, such ROI excludes the high compressive strain concentrations typical for the BDCN test i.e. top – load transition point and bottom – rigid support, which highly affects the crack/notch tip search algorithm.

3.5 Identification of a Traction-free Fracture Crack Tip

The crucial part of the DIC analysis is the correct identification of a traction-free crack tip. Therefore, in this study we propose an adjustment to the mode I traction-free crack methodology originally proposed by Chen et al. in [80]. Chen's methodology uses the horizontal displacement difference function $C(y)$, which is extracted from two equidistant parallel lines with origin at the notch tip. The traction-free crack is found at the location $C(y) \approx 0$ and $\partial C(y)/\partial y \approx 0$.

Unfortunately, this methodology was developed for tensile mode I cracks and for mixed-mode I/II cracks it generates high errors in the crack location. Therefore, our upgrade lies in a simple, yet effective transformation of the measured DIC displacements. Since the crack is opening under tensile load, that is perpendicular to the crack, we transform the measured DIC displacements *u* and *v* in the global coordinate system (CS) X-Y into the local CS X_1-Y_1 with origin at the notch tip and the local vertical axis Y_1 runs parallel to the crack. The transformation uses an angle γ with a counter clockwise direction. The transformation from global X-Y to X_1-Y_1 local coordinate system is shown in Figure 10(a).

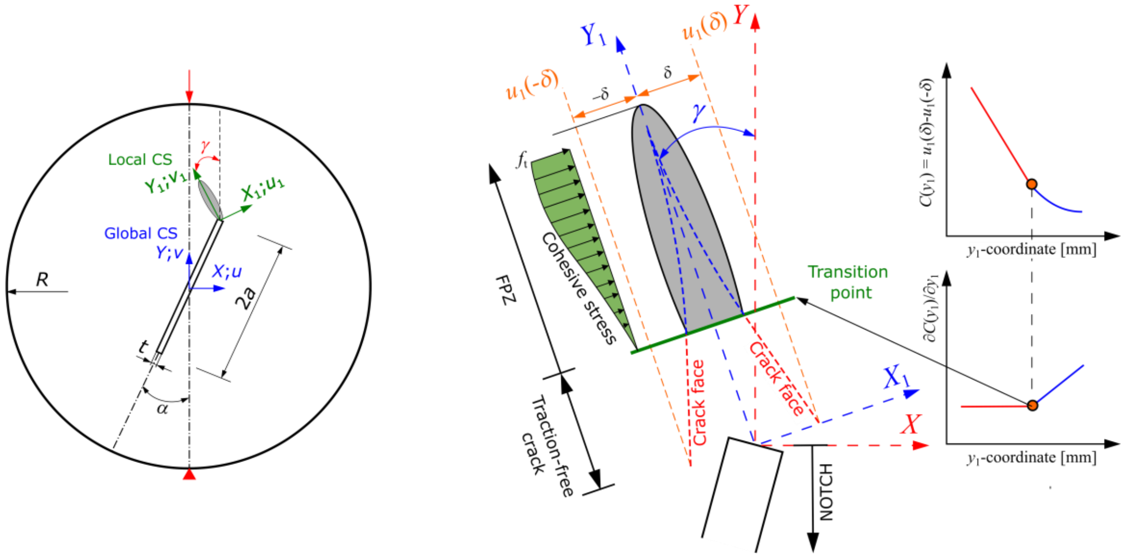

(a) (b)

Figure 10: Transformation of a crack tip displacements to a local coordinate system X_1-Y_1 (a) and (b) - adjustment of the traction-free crack localisation for mixed-mode I/II load conditions.

Based on the transformation from Figure 10(a), displacements u_1 are the crack opening and displacements v_1 are the crack sliding displacements and are directly related to mode I and mode II loading, respectively. Then the traction-free crack identification, as proposed by Chen et al., can be used to localise the mixed-mode I/II load in the local CS X_1-Y_1 with the use of horizontal displacements $u_1(y)$. The proposed changes from mode I to mixed-mode I/II crack identification are schematically presented in Figure 10(b).

The novel traction-free crack identification can be achieved by following the same steps, but this time in the local CS X_1-Y_1. The horizontal displacement difference function is obtained as $C(y_1) = u_1(\delta)$-$u_1(-\delta)$. The distance δ from the crack remains same as for the mode I cracks. Similarly to the global CS X-Y, the traction-free crack is obtained when $C(y_1) \approx 0$ and $\partial C(y_1)/\partial y_1 \approx 0$. These two coordinate systems are linearly transformed, thus the displacements gradients are also linearly related [38]. Therefore, the above-mentioned methodology is valid for mixed-mode I/II load conditions.

The FPZ is then located ahead of the traction-free crack as schematically represented by the grey area resembled by an ellipsoid in Figure 10. The size of this FPZ/ellipsoid is usually identified by its length l_{FPZ} and its width w, which both can serve as a major and minor axis of the ellipse.

4. Estimation of the FPZ Size ahead of Notch

Since the FPZ is a typical material property for concrete, its estimation ahead of the notch tip plays a crucial role in the fracture process. In what follows, we present two available methods for FPZ estimation and we discuss their applicability to concrete as well as to the DIC experimental data. The first method is based on the analytical estimation of the tensile modulus and the other one is based on the LEFM theory.

4.1 Estimation of the FPZ Extension Based on Tensile Modulus

Once the traction-free crack is identified, the FPZ extension ahead of the crack has to be localised and analysed. The FPZ is present in the concrete once the local stresses ahead of the notch reach the material strength f_t, resulting in multiple micro-cracks located around the macro-crack.

In the methodology mentioned above, for mode I Chen identified the FPZ by using a strain envelope around the traction-free crack [80]. This strain envelope is based on the indirect measurement of the tensile modulus E_t prosed by Jianhong [81]. Jianhong's measurement of the tensile modulus E_t was done on the Brazilian disc specimens with a strain gauge placed in the centre of the disc to measure the transverse strain ε_{xx}. Thus, the measurement of the tensile modulus E_t is done from a compressive test and the analytical formulas to obtain its value are shown in Eqs. (10)-(12).

$$E_t = AE_S = A\frac{2P}{\pi DB\varepsilon_{xx}} \tag{10}$$

where E_s is the splitting elastic modulus from the measured stress–strain diagram, D is the disc's diameter, L is the half-length of the strain gauge, v is the Poisson's ratio, P the concentrated load, B is the disc's thickness, ε_{xx} is the transversal strain at the centre of the disc and A is the correction coefficient and has the following form:

$$A = \left(1 - \frac{D}{L}\,arctan\left(\frac{2L}{D}\right)\right)(1-\nu) + \frac{2D^2(1+\nu)}{4L^2 + D^2}. \tag{11}$$

In his paper Chen [80], relates the critical strain $\varepsilon_{xx,c}$ and its envelope to a rather empirical formulation, which can be expressed as:

$$\varepsilon_{xx,C} = \frac{\sigma_t}{E_t} = \frac{\sigma_t}{0.72E_C} \tag{12}$$

The reduction of the compressive modulus E_c by 28% in Eq. (12) is based on the experimental measurement of sandstone, which has different inner structure compared to concrete.

Another setback for the use of only 72% of the compressive modulus E_C is that this value was interpolated from other rock materials and is used in a 3PB test configuration instead on the BDCN test specimen, which might lead to misleading results. Additionally, Eq. (12) calculates a strain $\varepsilon_{xx,c}$, which is in the direction of the global X-axis and it is more suitable to find an application for mode I FPZ size estimations. Nonetheless, this value of transverse strain calculated from Eq. (12) may serve as an initial and indicative value for the strain envelope ahead of the traction-free crack.

4.2 Estimation of FPZ Extension Based on Critical Tangential Strain

Since the BDCN geometry possess an initial notch and the load-displacement P-δ diagram witness a brittle failure (the P-δ diagram does not show a post-peak softening branch). This suggests using LEFM approach to analyse experimentally measured strains and displacement fields. However, the measured DIC strain maps ahead of the notch tip are in contradiction with this statement as the development of the FPZ was observed. Therefore, the LEFM can be used at greater distances from the crack tip to provide correct stress and strains estimations [53,82]. Accordingly, no strain data were employed in the analysis from the region within the pre-notch.

This can be achieved by using a two-parameter LEFM (K-T) formulation of the strain fields around the crack tip. The K-T LEFM approach, allows for assessment of the strain envelope around the traction-free crack by calculation of the tangential strain $\varepsilon_{\theta\theta}$ as presented in Eq. (3). Moreover, a critical tangential strain $\varepsilon_{\theta\theta,C}$ for which brittle failure occurs is achieved by substitution of the material's fracture toughness for mode I and mode II into Eq.(3). The critical tangential strain $\varepsilon_{\theta\theta,C}$ can be calculated as follows:

$$\varepsilon_{\theta\theta,C} = \frac{K_{IC}}{E\sqrt{2\pi r_C}}(f_{\theta\theta} - \nu f_{rr}) + \frac{K_{IIC}}{E\sqrt{2\pi r_C}}(g_{\theta\theta} - \nu g_{rr}) + \frac{T_C}{E}(sin^2\theta - \nu cos^2\theta) \tag{13}$$

where K_{IC} and K_{IIC} are the material fracture toughness for mode I and mode II, respectively, T_C is the value of T-stress corresponding to the maximum load and r_C is the critical distance. Besides materials parameters K_{IC}, K_{IIC} and T_C another governing parameter for correct prediction of brittle failure in Eq. (13) is the critical distance r_C.

The critical distance r_C is a material parameter which expresses the distance from the notch tip in which the crack opening stress exceeds the material's yielding or for concrete the tensile strength. The critical distance was originally derived to represent the plastic zone length ahead of the crack tip and was introduced by Irwin [83] as follows:

$$r_C = \frac{1}{2p}\left(\frac{K_{IC}}{\sigma_t}\right)^2 \text{ – plane stress,} \tag{14}$$

$$r_C = \frac{1}{6p}\left(\frac{K_{IC}}{\sigma_t}\right)^2 \text{ – plane strain.} \tag{15}$$

where σ_t is the tensile strength.

The original plastic zone length as derived by Irwin has been adopted for concrete materials for which it is often referred to as the characteristic length L_{ch} and it is proportional to the size of the FPZ. Hillerborg et al. [4] formulated the characteristic length L_{ch} by using a fictious crack model as:

$$L_{ch} = \left(\frac{K_{IC}}{\sigma_t}\right)^2. \tag{16}$$

Later, Karihaloo [7] argued that the characteristic length L_{ch} can be estimated as:

$$L_{ch} = \frac{1}{p}\left(\frac{K_{IC}}{\sigma_t}\right)^2. \tag{17}$$

These above-mentioned formulas used for the estimation of the FPZ size use the fracture toughness K_{IC}, which is related to the first WE term. Ayatollahi and Akbardoost [84] have recently postulated a method to determinate the critical distance r_C by using the third term of WE: A_{3C}. Moreover, they showed its size independency for concrete. In addition to these formulas, Otsuka [85] referred the size of the FPZ as the maximum aggregate size d_{agg}, while Bažant [86] relates the FPZ size to variation of d_{agg} that lies in the interval from d_{agg} to 12 × d_{agg}. This connection to aggregate size was recently studied by Alanazi & Susmel in [87] for both static and cyclic loads unveiling a good prediction of the failure of the specimen.

An overview of the FPZ size estimation by using analytical Eqs. (14)-(17) with the input from previously measured fracture toughness K_{IC} (presented in Table 3), is given in Table 5.

Table 5: Estimation of FPZ length based on different approaches.

Test type	Tensile strength f_t [MPa]	r_C [mm] - plane stress (Eq. (14))	r_C [mm] - plane strain (Eq. (15))	L_{ch} [mm] - (Eq. (16))	L_{ch} [mm] - (Eq. (17))	d_{agg} [mm]
Flexural 3PB test	6.30	3.79	1.26	23.81	7.58	8

Since the critical distance r_C is one of the governing parameters in Eq. (13), the critical tangential strain $\varepsilon_{\theta\theta,C}$ value will vary accordingly. Similar to the critical distance r_C, the T-stress plays a key role in the estimation of the critical tangential strain $\varepsilon_{\theta\theta,C}$. In this study, a Young's modulus E = 41 GPa and a Poisson's ratio of 0.2 were used to calculate tangential strain $\varepsilon_{\theta\theta}$.

Thus, Figure 11(a) shows the tangential strain $\varepsilon_{\theta\theta}$ calculated by using only the SIF in Eq.(13) and Figure 11(b) shows the tangential strain $\varepsilon_{\theta\theta}$ using the K-T formulation in Eq. (13) for pure mode II load conditions together with various values of the critical distance r_C.

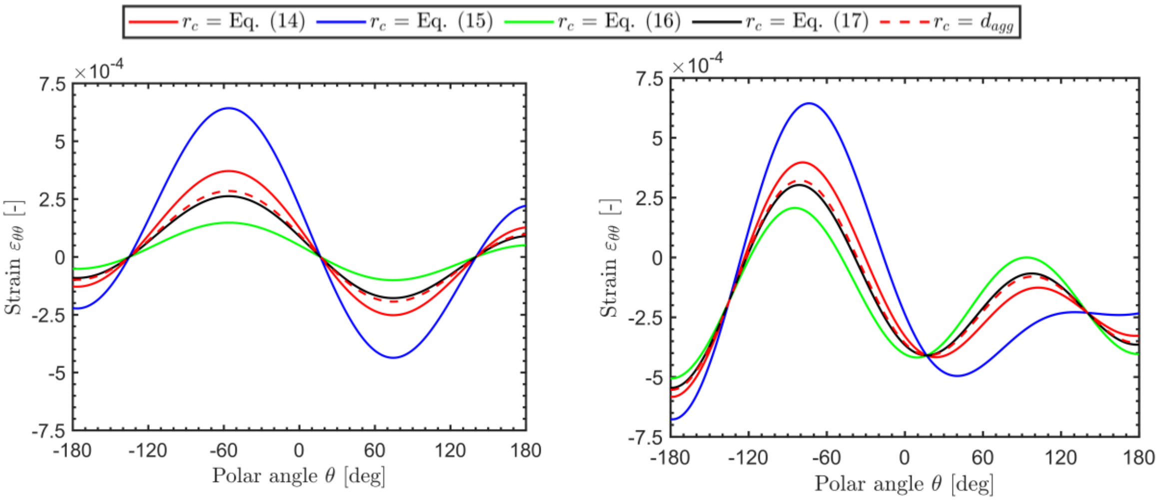

(a) (b)

Figure 11: Comparison of critical tangential stain $\varepsilon_{\theta\theta,\mathrm{C}}$ curves using 3PB flexural strength for notch inclination angle $\alpha = 27°$ and relative notch length $a/R = 0.267$, (a) – SIFs description (b) – SIFs + *T*-stress description.

As can be seen in Figure 11, the highest tangential strain $\varepsilon_{\theta\theta}$ for both cases is achieved using the critical distance r_C calculated by Eq.(15). This is in agreement with the general expectation that the strain, similarly to the stress, will increase in value with a decreasing value of r_C. Conversely, the lowest value of $\varepsilon_{\theta\theta}$ is attained by using Eq.(16) for its estimation i.e., the highest value of r_C. The rest of the estimated values of tangential strain $\varepsilon_{\theta\theta}$ curves lie in between these two limit values.

In order to estimate the extent of FPZ from the traction-free crack, the maximum value of strain $\varepsilon_{\theta\theta}$ as presented in Figure 11 will serve as its critical value $\varepsilon_{\theta\theta,\mathrm{C}}$. In the following table, a comparison of such values obtained for both *K*-*T* formulation is given together with the empirical value of $\varepsilon_{xx,\mathrm{C}}$ as presented in Eq. (12).

Table 6: Values of critical tangential strain $\varepsilon_{\theta\theta,\mathrm{C}}$ based on various values of critical distance r_C and material's tensile strength.

Test type	$\varepsilon_{\theta\theta,\mathrm{C}}$ [-] × 10^{-4}					
	$\frac{\sigma_t}{0.72E_C}$ (Eq. (12))	r_C (Eq.(14))	r_C (Eq.(15))	L_ch (Eq.(16))	L_ch (Eq.(17))	d_agg
Flexural 3PB test	2.178	3.973	6.441	2.069	3.027	3.219

The values of critical tangential strain $\varepsilon_{\theta\theta,\mathrm{C}}$ again follow the observation made in Figure 11, i.e. the highest values of $\varepsilon_{\theta\theta,\mathrm{C}}$ are found for the lowest value of critical distance r_C and vice versa. Additionally, the positive value of tangential strain $\varepsilon_{\theta\theta}$ component represents a crack opening strain for any mode combinations of load, while the negative value of $\varepsilon_{\theta\theta}$ strain is crack closing strain. Consequently, the positive value of $\varepsilon_{\theta\theta}$ strains will be used as the cracks are mainly initiating for tensile loads. This is valuable especially for mixed-mode I/II cracks, where it is necessary to distinguish the contribution of each loading mode on the crack initiation process.

5. Results and Discussion

In this section we give a comprehensive overview of the experimental results. We begin with the presentation of two independent FPZ evolutions during the BDCN test under the mixed-mode I/II loading. Afterwards, we present in detail an upgrade of traction-free crack localisation method based on the methodology for mode I cracks. Thereafter, we present and discuss the experimental results of localised traction-free cracks and FPZ extent. Finally, we propose an adjustment to the analytical formulas used in the prediction of the FPZ length based on the effective fracture toughness $K_{\mathrm{C,EFF}}$. This is complemented with an overview of measured FPZ properties i.e., its length l_FPZ and measured crack vector components CTOD and CTSD.

5.1 FPZ Evolution under Mixed-Mode I/II

Since the FPZ is often investigated for mode I load conditions, its evolution under mixed-mode I/II is presented. The measured load-displacement *P-d* diagram of a BDCN specimen shows a linear elastic behaviour up to 55% of the maximum load. The DIC data acquisition starts after reaching this value, as the crack and the FPZ start to develop. Since the BDCN geometry has a notch placed in the centre of the disc, the crack and the consequent FPZ can be observed at both notch ends, i.e., top – closer to the applied load and bottom – closer to the rigid support. Thus, this experimental test delivers twice as much information to analyse the FPZ as a 3PB test. The captured FPZ evolution during BDCN test is presented in Figure 12.

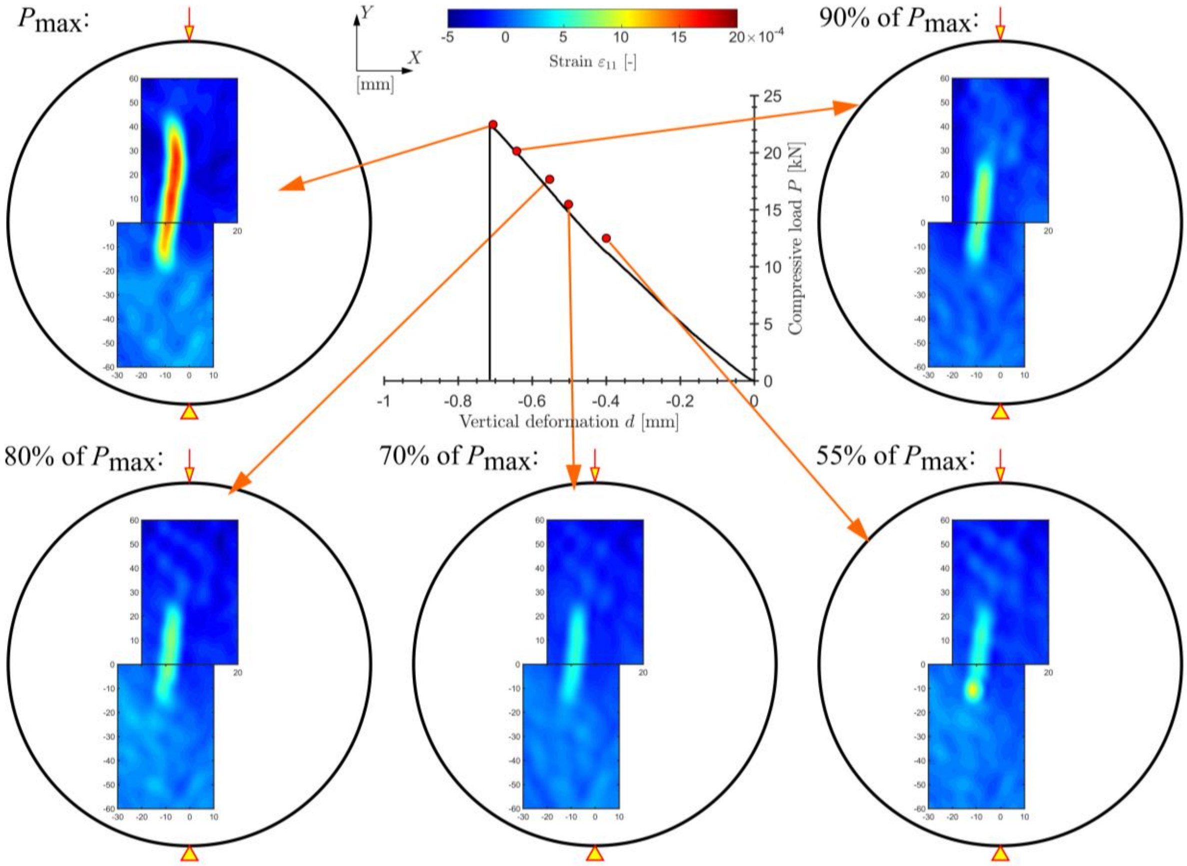

Figure 12: Development of principal strain ε_{11} and localization of the FPZ under mixed-mode I/II load ($a/R = 0.4$ $\alpha = 15°$)

A deflection/shift of the FPZ from the vertical path towards the loading point (top edge of the disc) can be observed in Figure 12. This observation follows the assumption made in Figure 1. Not only the typical crack deflection under the mixed-mode I/II load, but an asymmetric development of FPZ from both notch ends can be observed here as well. The crack deflection is related to mode II presence as discussed earlier in this paper, while the retarded FPZ development can be related to the heterogenic structure of concrete. The crack/FPZ retardation can be linked with coarse aggregates with a size up to 8 mm. This can lead to local crack arrest as the aggregates have better mechanical properties than the surrounding cement matrix and the crack has to overcome a longer distance around the aggregate, which later on can increase the load capacity. Afterwards, the crack has to propagate with a higher speed due to the accumulated energy in the specimen, which results in a typical splitting behaviour of the test.

The utilization of the DIC technique for the BDCN test allowed to observe a typical quasi-brittle behaviour of concrete, which is unique for this test as the *P-d* diagram (Figure 12) shows the brittle behaviour of the test, i.e., the specimen fails after reaching the maximum load without typical post-peak softening branch. Good time resolution was achieved to identify the peak load by performing the test at a relatively low speed (0.01 mm/s) and employing a fast camera (150 FPS). To the authors knowledge, this is the first time a FPZ was not only observed but comprehensively analysed. Based on this newly observed quasi-brittle behaviour, we believe that the BDCN test could be used in the measurement of the fracture energy G_f, which may find a practical application in the analysis of the renovated structures. This could be achieved by measuring the CMOD during the test and by calculating the fracture energy G_f based on the current methods [88]. However, the measurement of the fracture energy G_f from this test is a complex problem and lies beyond the scope of this work.

5.2 Traction-free Crack and FPZ Extension

To illustrate the upgrade to the mixed-mode I/II of the traction-free crack localisation methodology, we have selected a specimen with $a/R = 0.4$ and an angle $\alpha = 15°$ to achieve mixed-mode I/II loading. The DIC analysis was performed on the displacement and strain maps captured at maximum load. For simplicity reasons, we show only the analysed ROI of the top notch (see Figure 9). The same methodology was used for ROI at the bottom notch.

To localise the traction-free crack tip and to demonstrate the adjustments to the methodology used for mode I cracks, two lines are placed from the centre of the disc on the left and right side with a distance $\delta = 2.5$ mm (the distance between them is $2\delta = 5$ mm). Afterwards, these two lines are inclined by an angle $\gamma = 18°$. This angle γ serves as a transformation angle from the global X-Y CS to the local CS X_1-Y_1. After preparation of the DIC data, a horizontal displacement u_1 can be extracted and used to calculate the displacement difference function $C(y_1)$. This process of traction-free crack tip localisation together with its found location is illustrated in Figure 13.

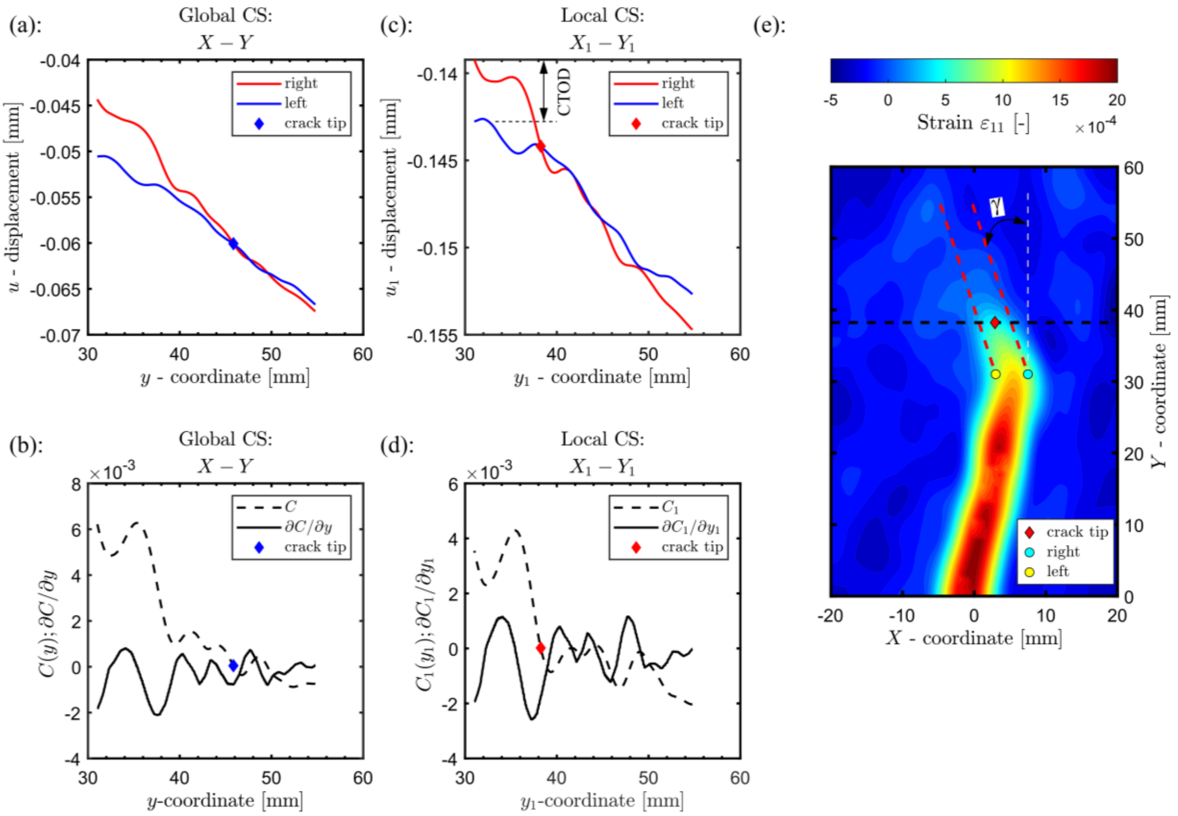

Figure 13: Traction-free crack localization process under mixed-mode I/II load (a) - displacement u in the global CS, (b) - function $C(y)$ and its derivation $\partial C(y)/\partial y$ in the global CS X-Y, (c) - displacement u_1 in the local CS X_1-Y_1, (d) - function $C(y_1)$ and its derivation $\partial C(y_1)/\partial y_1$ in the local CS X_1-Y_1 and (e) - location of the traction free crack in ε_{11} strain map.

A clear difference can be observed in the extracted displacements in the global X-Y (Figure 13(a)-(b)) and in the local X_1-Y_1 (Figure 13(c)-(d)) CS. Furthermore, a misinterpretation of the traction-free crack length can be observed, if the displacement u in the global CS X-Y was be used for mixed-mode I/II crack localisation. This difference in the crack length is due to the presence of mode II displacements v

acting in the direction of the global *X*-axis, while in the case of the local coordinate these two displacement components u_1 and v_1, mode I and mode II, act separately in the local CS. Thus, this transformation allows for a clear estimation of the values of crack CTOD and CTSD to determine the key role of each loading mode in the cracking process under mixed mode I/II load conditions. Although the CTOD is normally used as a fracture parameter, the measurement of CTSD as an additional fracture parameter appears to be very useful to improve the crack tip information [39,40].

The location of the traction-free crack obtained from DIC displacement maps together with the lines used for displacements extraction is shown in a principal strain map ε_{11}. Such presentation of a crack tip location in the principal strain ε_{11} map clearly illustrates the presence and size of the FPZ ahead of the crack tip. Additionally, this plot shows the location of the points at which the CTOD and CTSD values were obtained.

The overestimation of the traction-free crack and the FPZ size can be seen in the DIC strain maps. This effect becomes more evident when comparing the strains ε_{xx} of the global *X*-axis and the principal strains ε_{11}. The comparison of these to strain components is shown in Figure 14.

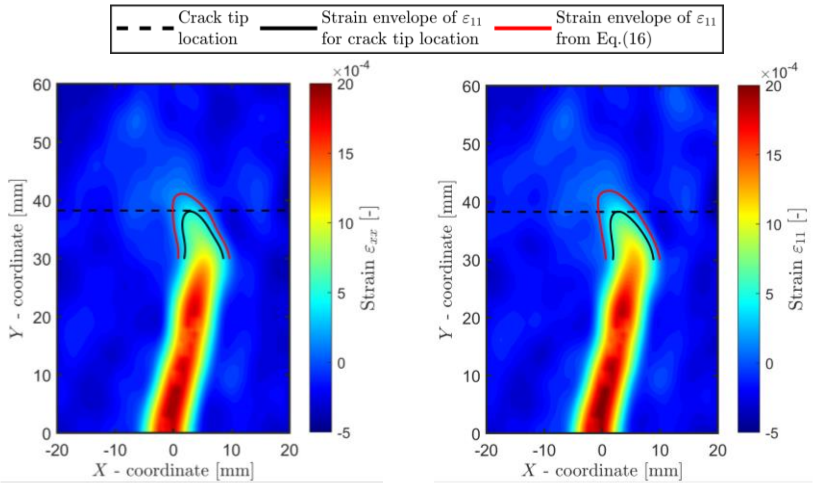

(a) (b)

Figure 14: Comparison of measured DIC strains for maximum load – (a) ε_{xx} and (b) ε_{11} together with the traction-free crack and FPZ extend.

Careful observation of Figure 14(b) shows a minor change in the ε_{11} strain map located on the top right hand side around coordinates $x = 15$ and $y = 58$ can be seen. This is the location of a typical secondary crack with the origin at the point the load is transferred to the BDCN specimen. This secondary crack leads to stress/strains concentrations and this is the reason to use ROI in further DIC crack analysis. Nonetheless, these high stress/strain concentrations do not affect the strains condition in the vicinity of the notch tip.

Another interesting observation from the principal strains ε_{11} map as presented in Figure 14(b) can be made when compared to lateral ε_{xx} strain map in Figure 14(a). The ε_{11} map shows area with lower values ahead of the traction-free crack tip extending to a wider region towards the loading point (around $x = 0$ any $y = 45$), which indicates possible crack branching. The measured strain ε_{xx} map shows this region with similar values of strain at a further distance from the traction-free crack. This difference is again due to unconsidered action of vertical deformations in the ε_{xx} strains. Therefore, we will use the principal strains ε_{11} in further analysis of FPZ.

Besides strain maps of ε_{11}, a traction-free crack presence can be demonstrated by a typical singularity in the captured horizontal displacement field *u*. Thus, the presence of the traction-free crack ahead of the notch can be observed as a change of the horizontal displacements $u(x)$ along the *X*-coordinate, which can be extracted from various vertical positions along the disc's radius i.e. different *Y*-coordinates. The selected locations used of the extraction of the $u(x)$ are showed in captured horizontal displacement *u* map in Figure 15(a) for the top notch position, while the development of the horizontal displacement $u(x)$ extracted at various vertical locations is shown in Figure 15(b).

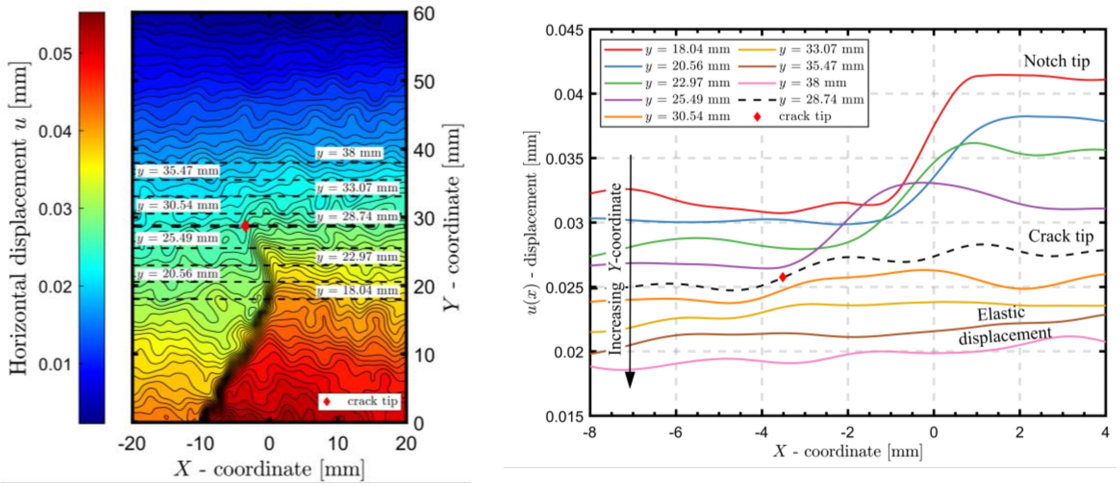

(a) (b)

Figure 15: Traction-free crack location showed in captured horizontal displacement u map - (a) and (b) - the development of the horizontal displacement $u(x)$ for a different vertical (Y-coordinates) locations.

A typical crack discontinuity located ahead of the notch tip in horizontal displacement u map is shown in Figure 15(a). Such discontinuity is more clearly visible in Figure 15(b), where it is represented as a rapid increase in the displacement $u(x)$ value extracted at various Y-coordinates that is computed as a gradient. This discontinuity, i.e. the crack, is declining with an increasing Y-coordinate due to undeveloped crack and FPZ in the specimen’s ligament ahead of the notch tip. The gradient threshold to identify the crack tip was selected to be 2.4×10^{-3}. Additionally, in Figure 15(b), typical properties of horizontal displacement u fields with a crack are illustrated, i.e., notch tip, traction-free crack and a typical evolution of the elastic displacement u, which is present ahead of the FPZ without crack presence [80].

5.3 Traction-free Crack and FPZ under Mixed-mode I/II

The adjusted methodology for the traction-free crack localisation can be used for other angles α, and since the BDCN specimen has two FPZs ahead of each notch tip, it can be used separately for both the top and bottom notch analysis. The FPZ is presented as a principal strain ε_{11} envelope for the value of approx. 2×10^{-4} as presented in Table 6 Eq. (13). A similar value of the critical strain and the FPZ extension before specimen’s failure was reported by Das et. al [16], which uses for the DIC strain analysis a normal distribution, representing the size of the FPZ instead of strain envelope of certain value. Localised traction-free cracks with the FPZ extent for the top notch region for a relative notch length a/R = 0.267 are presented in Figure 16 and for a/R = 0.4 in Figure 17.

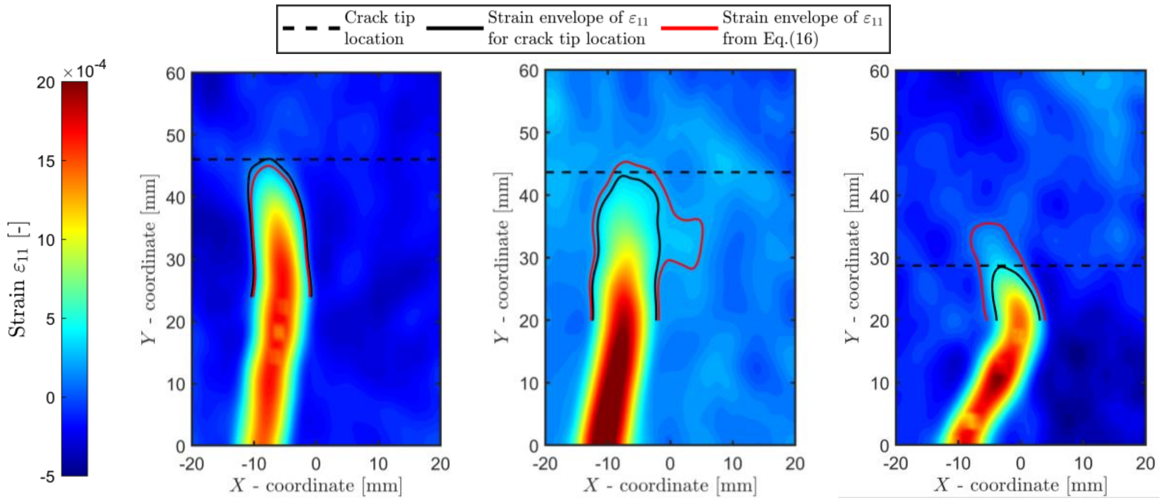

(a) (b) (c)

Figure 16: Comparison of top notch DIC measured ε_{11} strains measured for maximum load with the traction-free crack location and FPZ extent for $a/R = 0.267$ – (a) $\alpha = 5°$, (b) $\alpha = 10°$ and (c) $\alpha = 27°$.

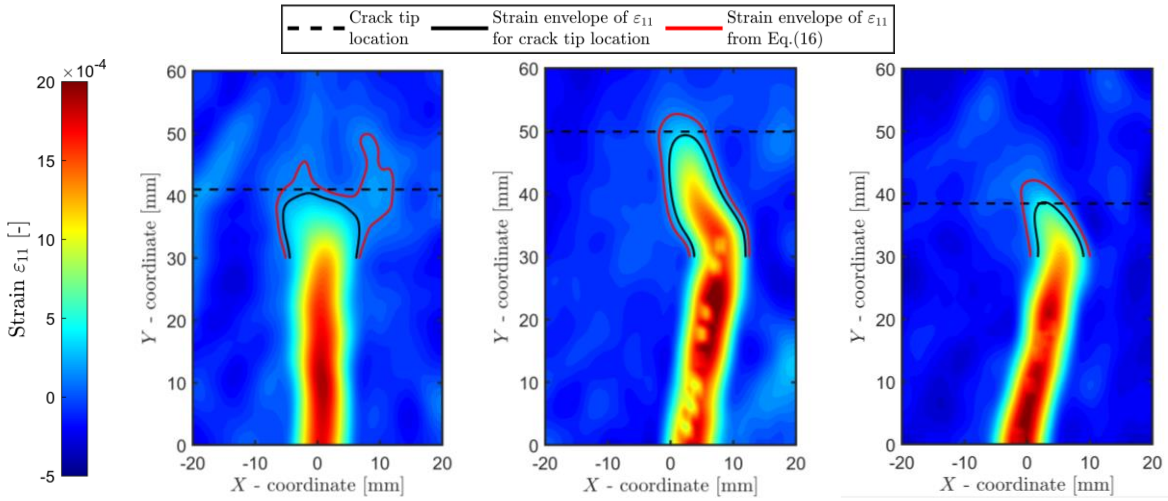

(a) (b) (c)

Figure 17: Comparison of top notch DIC measured ε_{11} strains measured for maximum load with the traction-free crack location and FPZ extent for $a/R = 0.4$ – (a) $\alpha = 0°$, (b) $\alpha = 5°$ and (c) $\alpha = 15°$.

From both figures Figure 16 and Figure 17 various traction-free crack locations and a variety of FPZ sizes and shapes can be seen. Generally, the cracks as well as the FPZ for the dominant mode I load, show the length to be approx. 20 mm, while the cracks for a dominant mode II load show a FPZ with almost half its size, i.e. 12 mm.

An interesting observation in Figure 16(a) is that the strain envelope equivalent for the value of a traction-free crack is higher than the strain based on Eq. (13). This is due to the fact that the localised crack is longer that the estimated strain envelope for the FPZ extent based on the LEFM. This suggests that a higher value of the critical distance r_C in Eq. (13) should be used. Additionally, the strain envelope for the FPZ extent shows irregular shapes in Figure 16(b) and in Figure 17(a). This indicates possible crack branching due to the presence of an aggregate ahead of the traction-free crack/FPZ. Similar behaviour was previously observed [16,80].

Similarly to the region of the top notch, the region of the bottom notch can be analysed in the same way. Localised traction-free cracks and FPZ extent for the bottom notch region, for a relative notch length $a/R = 0.267$, are presented in Figure 18 and for $a/R = 0.4$, in Figure 19. Please note that the results for $a/R = 0.4$ $\alpha = 0°$ and 5° have ROI adjusted by 10 mm in the X-direction by 10 mm due to a crack presence outside of the ROI mentioned in Figure 9.

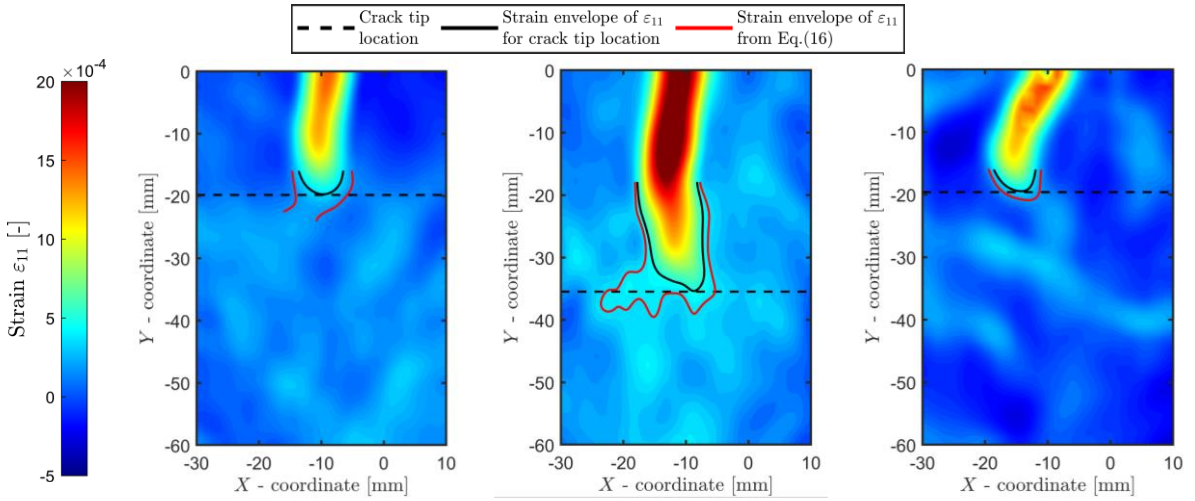

(a) (b) (c)

Figure 18: Comparison of bottom notch DIC measured ε_{11} strains measured for maximum load with the traction-free crack location and FPZ extent for a/R = 0.267 – (a) $\alpha = 5°$, (b) $\alpha = 10°$ and (c) $\alpha = 27°$.

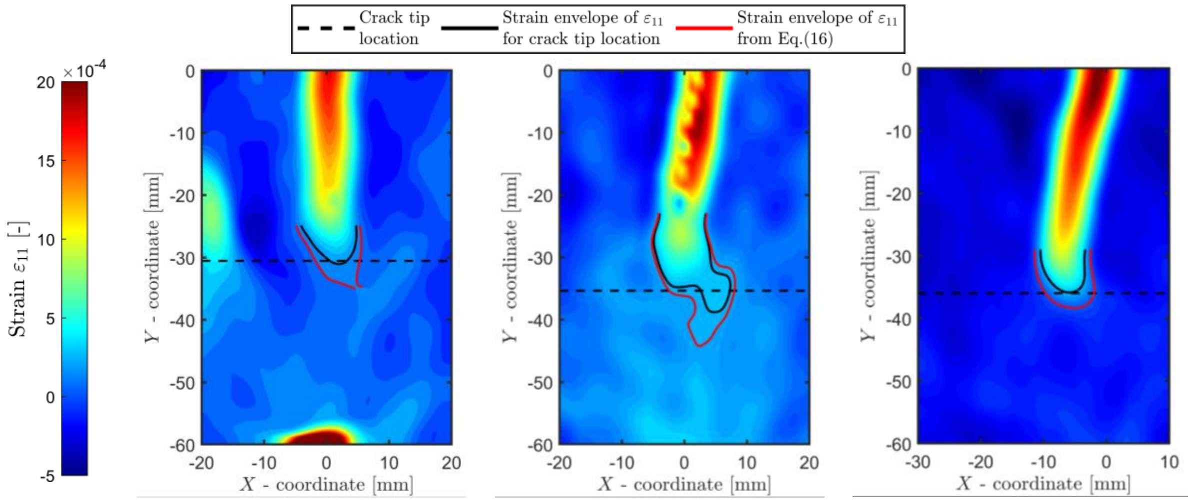

(a) (b) (c)

Figure 19: Comparison of bottom notch DIC measured ε_{11} strains measured for maximum load with the traction-free crack location and FPZ extent for a/R = 0.4 – (a) $\alpha = 0°$, (b) $\alpha = 5°$ and (c) $\alpha = 15°$.

Both Figure 18 and Figure 19 show similar results for the traction-free crack and FPZ extent as were observed for the top notch region. Irregular strain envelope for the estimated FPZ size can again be observed in Figure 18(b) Figure 19(a) and Figure 19(b) as the crack branches around the aggregates. Moreover, Figure 18(b) indicates a crack initiation and propagation towards the left hand side instead of the bottom location, which serves as a rigid support. This follows the observation made in Figure 16(b), in which the crack starts to kink to the right hand side instead of propagating directly towards the loading point (upper edge of the ROI located at Y = 60 mm). This observed crack branching can be caused by presence of pores or due to weaker links between the cement paste and the coarse aggregate.

Additionally, the strain map and strain envelope presented in Figure 19(a) i.e. pure mode I, shows high strain concentrations around the location of the rigid support (y = -60 mm). This strain concentration indicates possible crack initiation from this location, which is a typical implication of the BCDN test, prior to the specimen failure as a secondary crack can be observed here due to locking of the specimen in the testing jaws.

Moreover, this difference in the size of the FPZ size increases with increasing mode II dominance, for which the size of the FPZ is significantly lower than for the cases closer to pure mode I load conditions (see Figure 16(c) and Figure 17(c)). This reduction of the FPZ size can be caused by shear interlock of the aggregates in the cracked material, which leads to a lower vertical deformation as well as to a reduction of the transverse displacement acting as a crack opening. Another reason may be the presence of a coarse aggregate ahead of the crack tip, which can cause crack arrest as it is believed to have a higher tensile strength than the surrounding cement matrix.

5.4 FPZ Properties under Mixed Mode I/II

Since the DIC strain maps show different sizes of the FPZ for various mode-mixity I/II conditions, it is crucial to separately analyse the crack opening and sliding to verify such statements. For this, the CTOD and the CTSD components were measured at the location schematically indicated in Figure 13(e). CTOD and CTSD crack components were obtained as a difference in local displacement u_1 and v_1, respectively. The determined values of CTOD and CTSD for various mode-mixity are presented in Table 7 for the top notch, while Table 8 presents values obtained for the bottom notch. Both tables present FPZ lengths as a distance from the notch tip to the traction-free crack tip location.

Table 7: Overview of measured CTOD and CTSD together with the FPZ length for top notch and for various mixed-mode I/II conditions.

Relative notch length a/R [-]	Notch inclination angle α [°]	Mode-mixity M^e [-]	CTOD [μm]	CTSD [μm]	CTSD/CTOD [-]	FPZ length l_{FPZ} [mm]
0.267	5	0.766	8.641	12.457	1.44	22.833
0.267	10	0.552	9.74	6.939	0.71	24.599
0.267	27	0.0	5.236	16.293	3.11	10.841
0.4	0	1.0	8.825	5.071	0.57	12
0.4	5	0.742	8.575	12.924	1.51	18.882
0.4	15	0.312	5.243	12.278	2.34	9.46

Table 8: Overview of measured CTOD and CTSD together with the FPZ length for bottom notch and for various mixed-mode I/II conditions.

Relative notch length a/R [-]	Notch inclination angle α [°]	Mode-mixity M^e [-]	CTOD [μm]	CTSD [μm]	CTSD/CTOD [-]	FPZ length l_{FPZ} [mm]
0.267	5	0.766	3.124	8.886	2.84	3.838
0.267	10	0.552	10.857	7.648	0.70	17.471
0.267	27	0.0	1.888	6.053	3.21	3.560
0.4	0	1.0	6.949	3.171	0.46	10.5411
0.4	5	0.742	6.760	9.269	1.37	12.351
0.4	15	0.312	4.004	10.471	2.62	6.951

The results of CTOD and CTSD as presented in Table 7 and Table 8, are in agreement with general expectation as for the mode I cracking the CTOD is predominant, while for the mode II crack the CTSD shows higher values than the CTOD. This validates observations from Figure 16, Figure 17, Figure 18 and Figure 19 that predicted the predominant fracture mode based on the strain map. It also provides valuable information about the mixed-mode I/II cracking process for concrete materials. The mode II dominance can be seen more clearly by looking at the CTSD/CTOD ratio (sixth column in Tables 7 and 8). Such a ratio appears to be an objective tool to predict the mode II dominance and its influence on the crack and FPZ development in concrete.

Both Table 7 and Table 8 present values of the FPZ size that vary with an increasing mixed-mode I/II load. All FPZ sizes are at least 10 times the DIC strain resolution, hence indicating that the current DIC setup is suitable for FPZ analysis in the current study. The size of the FPZ is larger for mode I cracks, while for mode II crack a significant size/length reduction is observed. Furthermore, if the FPZ size l_{FPZ} is compared with values presented in Table 5, a serious underestimation can be observed. These experimental results again confirm the inapplicability of the fundamental Irwin approach to the estimation of plastic zone r_c for concrete, as well as the Hillerborg's analytical formula for the estimations of characteristic length L_{ch}. Similarly to this, Bažant's empirical relation of the FPZ size to the maximum aggregate size d_{agg} is far from the measured lengths and provides misleading estimations for mixed-mode I/II cracks.

5.5 Improved Estimation of FPZ Length

To demonstrate the importance of the proposed change to the traditional analytical formulation of the calculation critical length r_C or characteristic length L_{ch}, we present here in this section an improved prediction of the FPZ size based on the effective fracture toughness $K_{C,EFF}$ as shown in Eq. (8). Both Table 7 and Table 8 show a significant difference in measured values of FPZ. This difference is more thoroughly observed, when the measured values are shown in a graph. A similar difference in CTOD and CSTD values was previously observed via numerical analysis by Miarka et. al [89]. For this reason, the measured values, as presented in Table 7 and in Table 8, are shown graphically together with their mean values for each studied *a*/*R* ratio. Figure 20(a) shows measured FPZ lengths related to the notch inclination angle α, while the Figure 20(b) shows measured FPZ lengths related to the mode mixity parameter M^e.

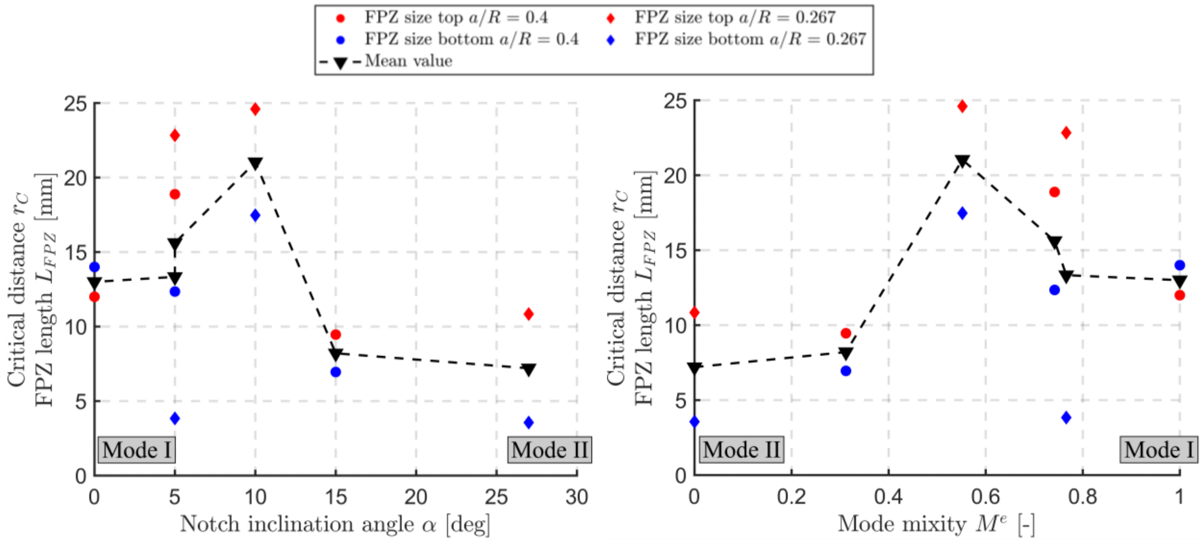

(a) (b)

Figure 20: Measured FPZ lengths against (a) - the notch inclination angle and (b) - Mode mixity parameter M^e.

An interesting trend of mean values, increasing with mode I dominance, can be observed in Figure 20. As it was mentioned earlier, relating the mixed-mode fracture analysis to a notch inclination angle α can provide misleading information as the stress conditions ahead of the notch tip vary based on the notch length. This misleading observation is clear in Figure 20(a), where the FPZ lengths are measured for the same angle $\alpha = 5°$, while in Figure 20(b) these values do not represent same mode mixity condition.

To capture this observed trend in Figure 20(b), an adjustment to Eq. (8) has to be made as the mode-mixity parameter M^e represents the horizontal axis and value of M^e equal to zero represents pure mode II. The reader is again referred to Appendix B – Effective Fracture Toughness for more details. This adjustments leads to following equation:

$$K_{C,EFF} = \sqrt{\left(K_{IC}\sin\left(\frac{90°}{\alpha_{II}}\alpha\right)\right)^2 + \left(K_{IIC}\cos\left(\frac{90°}{\alpha_{II}}\alpha\right)\right)^2}, \qquad (18)$$

Eq. (18) uses the same values of fracture toughness and α_{II} as Eq. (8). The calculated value of effective fracture toughness $K_{C,EFF}$ is then substituted to the classical relation for critical distance r_C or characteristic length L_{ch} as presented in Eqs. (14)-(17). This predicts the FPZ size in the whole range of studied mixed-mode I/II loading conditions similarly as it was shown for fracture forces P_C in Figure 6. The use of the mode II fracture toughness K_{IIC} in the prediction of the critical distance r_C with relatively good agreement between analytical predictions and experimental values was recently studied on PMMA material by Aminzadeh [90]. The predicted FPZ from our study sizes using Eq. (14) with the improved formulation for the effective fracture toughness $K_{C,EFF}$ are presented in Figure 21.

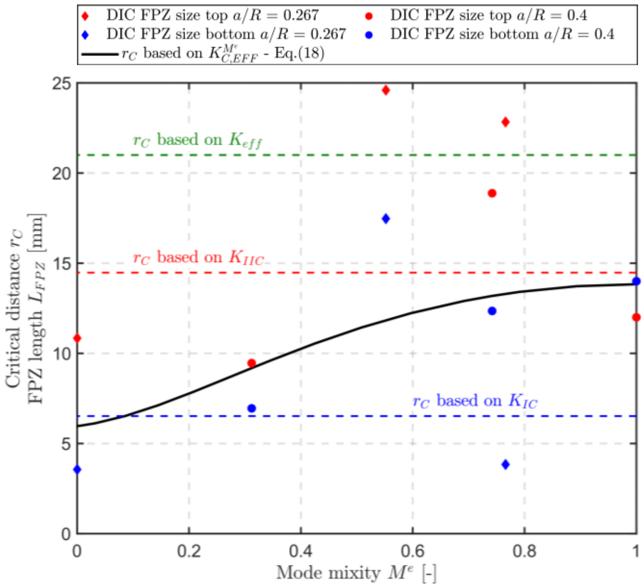

Figure 21: Comparison of various analytical approaches to predict FPZ size with experimentally measured data.

Figure 21 shows the predicted values of FPZ by using the effective fracture toughness $K^{M^e}_{C,EFF}$ from Eq. (18) with similar increasing values of mode I dominance as observed in Figure 20(b). Other values of FPZ lengths as calculated by using different values of fracture toughness K_{IC}, K_{IIC} and K_{eff} and also presented in Figure 20. As can be observed, the use of Eq. (18) allows for the prediction of the critical distance/FPZ length in the whole range of studied mixed-mode I/II conditions, while the other methods, predict a single value only.

This valuable prediction in the full range of mixed-mode I/II loading conditions can be verified further by showing the predicted values as calculated with Eq. (18) together with the measured and mean values. Such a comparison is presented in Figure 22.

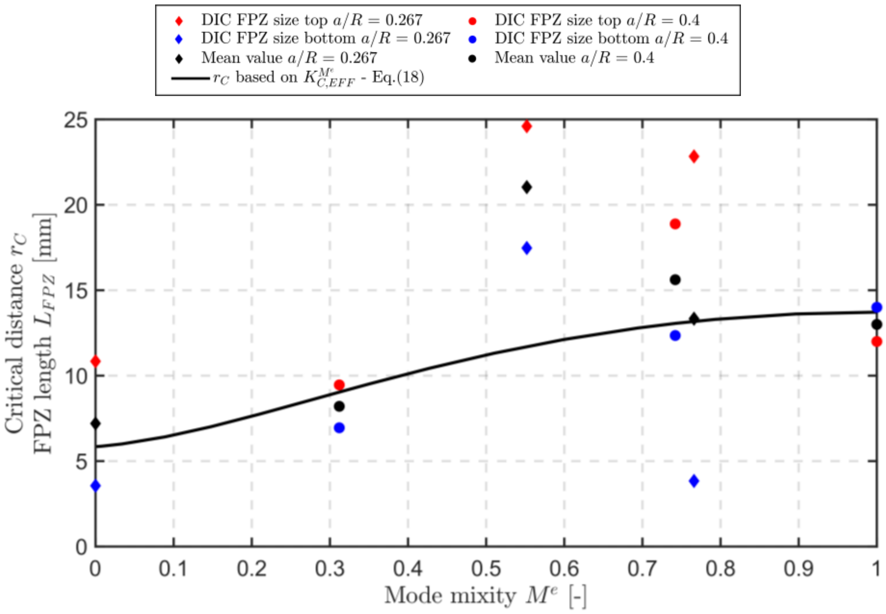

Figure 22: Comparison of experimentally measured FPZ size with analytically predicted values based on effective fracture toughness $K^{M^e}_{C,EFF}$.

From Figure 22 a clear improvement in the prediction of the FPZ size can be seen as the predicted values show a relatively small difference from the measured mean values. Additionally, this could be improved by using more BDCN specimens with different notch inclination angles α and relative notch length a/R. Lastly, it would be valuable to perform a size-effect study [91] on the use BDCN specimens in general, which is a research topic deserving more attention on its own. On the other hand, the proposed improvement for the calculation of the effective fracture toughness $K_{C,EFF}^{M^e}$ is only valid for the BDCN geometry, as it includes the angle α while other test specimens have completely different parameters.

However, based on the presented experimental results, we believe that the analysis of the mixed-mode I/II using the BDCN specimen could find more practical applications as it provides interesting and previously unseen results of FPZ properties. Finally, based on the results here, the BDCN specimen could find application in the assessment of fracture mechanical parameters of concrete structures prior to renovation.

Conclusions

This experimental study revisited the analysis of the fracture process zone (FPZ) in concrete, this time analysed by digital image correlation (DIC) analysis of displacements and strain fields captured on Brazilian disc specimens with central notch (BDCN) made from high performance concrete (HPC) under mixed mode I/II load conditions. In total, 6 specimens were analysed with various mixed-mode conditions ranging from pure mode I to pure mode II.

The experimentally captured DIC strains show a quasi-brittle behaviour of the BDCN specimen, which typically manifests brittle behaviour documented in the load deformation (P-d) diagram. The quasi-brittle behaviour is indicated by the presence of the FPZ with the origin at the notch tip. Moreover, the use of the BDCN specimen coupled with the DIC, allow to analyse two independent FPZ located at each notch end.

Traction-free cracks were localised by using an adjusted/novel methodology based on methods found in literature. The novel methodology presented in this paper allows for traction-free crack localization under the mixed-mode I/II load conditions as well as for pure mode I. Subsequently, the extension of the FPZ ahead of the crack tip was carried out based on the critical strains evaluated by an empirical formula and by the maximum tangential strain criterion based on the linear elastic fracture mechanics (LEFM). The results of the FPZ sizes were compared and a significant difference in size was observed for dominant mode II load conditions.

Furthermore, an analytical formula for the estimation of the FPZ size was presented, and its outcome was compared to experimental data. Additionally, it was demonstrated again that there exists a significant difference between analytical and experimental values of FPZ size for any mixed-mode I/II load condition. The traditional formulation of the FPZ length was improved to cover all mixed-mode I/II load conditions by the novel formulation of effective fracture toughness $K_{\mathrm{C,EFF}}$. This improvement was firstly demonstrated by back-calculation of fracture force P_{C} and by prediction of the FPZ size. To verify this statement, values of the crack tip opening (CTOD) and crack tip sliding displacements (CTSD) were extracted from the DIC displacement fields and compared. The CTOD and CTSD values again confirmed the observation for the FPZ sizes.

This experimental study showed the importance of the analysis of the mixed-mode I/II load condition i.e., a combination of tensile and shear, and its influence on the crack initiation and propagation together with its influence on the shape and size of the FPZ present ahead of the crack tip. Such a load condition is often omitted in research analysing the fracture behaviour of concrete.

Acknowledgements

Financial support provided by the Czech Science Foundation under project no. 21-08772S, as well as the Financial support of Programa Operativo FEDER from the Junta de Andalucia (Spain) through grant reference UMA18-FEDERJA-250 is also greatly acknowledged. Industrial support from Bettergy and

Dr Nicolas Ordonez is greatly acknowledged, as well as access to different structures and materials in the energy industry.

Appendix A – Williams' Expansion Functions

In Eq. (1) and in Eq. (3), functions f_{ij} and g_{ij} ($i,j = r,\theta$) are known function of angle θ as:

$$f_{rr} = \frac{1}{4}\left[5\cos\left(\frac{\theta}{2}\right) - \cos\left(\frac{3\theta}{2}\right)\right], \tag{A-1}$$

$$f_{\theta\theta} = \frac{1}{4}\left[3\cos\left(\frac{\theta}{2}\right) + \cos\left(\frac{3\theta}{2}\right)\right], \tag{A-2}$$

$$f_{r\theta} = \frac{1}{4}\left[\sin\left(\frac{\theta}{2}\right) + \sin\left(\frac{3\theta}{2}\right)\right], \tag{A-3}$$

$$g_{rr} = \frac{1}{4}\left[-5\sin\left(\frac{\theta}{2}\right) + 6\sin\left(\frac{3\theta}{2}\right)\right], \tag{A-4}$$

$$g_{\theta\theta} = \frac{1}{4}\left[-3\sin\left(\frac{\theta}{2}\right) - 3\sin\left(\frac{3\theta}{2}\right)\right], \tag{A-5}$$

$$g_{r\theta} = \frac{1}{4}\left[\cos\left(\frac{\theta}{2}\right) + 3\cos\left(\frac{3\theta}{2}\right)\right]. \tag{A-6}$$

Values of critical T-stress – T_C used in the calculation of critical tangential strain $\varepsilon_{\theta\theta,C}$ in Eq. (11) together with the maximum measured loads are showed in Table 9.

Table 9: Values of measured fracture forces and calculated values of critical T-stress T_c.

Specimen	Relative notch length a/R [-]	Notch inclination angle α [°]	P_{max} [kN]	T_c [MPa]
4_3_2	0.267	5	22.5	-22.692
4_3_3	0.267	10	24.33	-23.843
4_3_4	0.267	27	27.4	-19.411
6_3_1	0.4	0	13.09	-13.240
6_3_2	0.4	5	18.01	-17.644
6_3_3	0.4	15	17.22	-12.575

Appendix B – Effective Fracture Toughness

A BDCN specimen allows to test the fracture behaviour in the whole range of mixed mode I/II load conditions. Experimental results are usually evaluated using a fracture resistance curve based on mixed-mode I/II fracture criteria. The fracture resistance curve is assembled using relative coordinates as a ratio of the SIF to the mode I fracture toughness, i.e., K_I/K_{IC} for mode I and K_{II}/K_{IC} for mode II. In such a plot, mode I is shown on the horizontal axis, while mode II is shown on the vertical axis. The fracture resistance curve in relative coordinates shows similarity to an ellipse with the minor axis related to mode I, and the major axis related to mode II. Such a fracture resistance curve is schematically shown in Fig. B. 1.

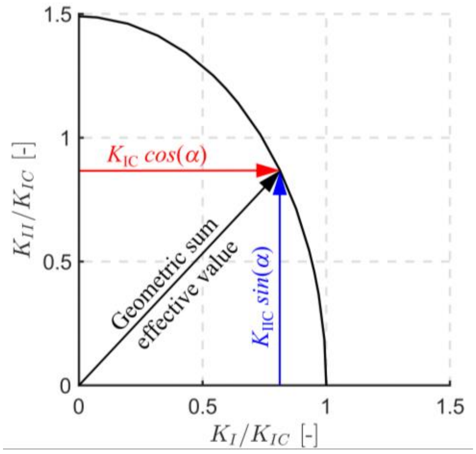

Fig. B. 1. Schematic representation of fracture resistance curve.

This ellipse in relative coordinates can be express mathematically as:

$$x = \frac{K_I}{K_{IC}} \cos(\alpha), \tag{B-1}$$

$$y = \frac{K_{II}}{K_{IC}} \sin(\alpha). \tag{B-2}$$

Since the pure mode II is present for different notch inclination angles α for every relative notch length a/R, a ratio of $90°/\alpha_{II}$ is added to Eqs. (B-1) and (B-2), which express the slope of the line in relative coordinates. Additionally, the relative coordinates can be simply transformed to express only value of the fracture toughness as:

$$x = K_{IC} \cos\left(\frac{90°}{\alpha_{II}} \alpha\right), \tag{B-3}$$

$$y = K_{IIC} \sin\left(\frac{90°}{\alpha_{II}} \alpha\right). \tag{B-4}$$

where α_{II} is the notch inclination angle for which the pure mode II is present.

Using the effective value of the SIF K_{EFF} (geometric sum) as presented in Eq. (4) by substitution of K_I with the x value from Eq. (B-3) and K_{II} with the y value from (B-4) one can obtain the effective fracture toughness $K_{C,EFF}$ as:

$$K_{C,EFF} = \sqrt{\left(K_{IC} \cos\left(\frac{90°}{\alpha_{II}} \alpha\right)\right)^2 + \left(K_{IIC} \sin\left(\frac{90°}{\alpha_{II}} \alpha\right)\right)^2}, \tag{B-5}$$

Using Eq. (B-5) fracture failure in the whole range of mixed-mode I/II load conditions can be predicted. To demonstrate the importance of Eq. (B-5) an adjustment to the earlier presented fracture resistance curve for mixed mode I/II failure is made by changin in the relative coordinates to SIF/$K_{C,EFF}$. This adjustment is demonstrated in Fig. B. 2 together with the fracture resistance curve in relative coordinates for mode I (SIF/K_{IC}) and in relative coordinates for mode II (SIF/K_{IIC}).

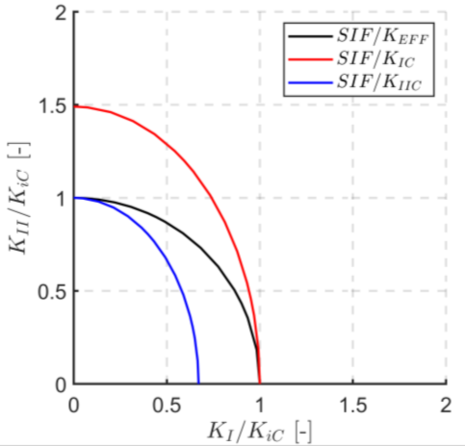

Fig. B. 2: Comparison of various relative coordinates to plot the fracture resistance curve.

Fracture resistance curves of SIF/K_{IC} or SIF/K_{IIC} are shown as ellipses in Fig. B. 2, while the adjusted fracture resistance curve SIF/$K_{C,EFF}$ ellipse changes to a circle. This change from ellipse to circle has an important practical application as it can predict fracture forces P_C and improve the fracture resistance to the whole range of mixed-mode I/II load conditions.

This change in Eq.(B-5) is related to the notch inclination angle α and to the angle α_{II} for pure mode II, which has values from 0 – mode I and larger than 0 for mode II (the specific values differ for different values of the ratio a/R). The relation of fracture resistance to the notch inclination angle α has some drawbacks, which are comprehensively discussed in this paper. Thus, a better illustration of the fracture process can be achieved by using the mode mixity parameter M^e. This change can be accounted in Eq. (B-5) by simply switching the horizontal and vertical axis since the mode mixity parameter M^e expresses mode II as zero and mode I as one. The adjustment from angle α to parameter M^e is:

$$K_{C,EFF} = \sqrt{\left(K_{IC}\sin\left(\frac{90°}{\alpha_{II}}\alpha\right)\right)^2 + \left(K_{IIC}\cos\left(\frac{90°}{\alpha_{II}}\alpha\right)\right)^2}, \tag{B-6}$$

References

[1] A. Carpinteri, Notch sensitivity in fracture testing of aggregative materials, Eng Fract Mech. 16 (1982) 467–481. https://doi.org/10.1016/0013-7944(82)90127-8.

[2] J. Xiao, W. Li, Z. Sun, D.A. Lange, S.P. Shah, Properties of interfacial transition zones in recycled aggregate concrete tested by nanoindentation, Cem Concr Compos. 37 (2013) 276–292. https://doi.org/10.1016/J.CEMCONCOMP.2013.01.006.

[3] Z.P. Bažant, J. Planas, Fracture and Size Effect in Concrete and Other Quasibrittle Materials, Fracture and Size Effect in Concrete and Other Quasibrittle Materials. (2019). https://doi.org/10.1201/9780203756799/FRACTURE-SIZE-EFFECT-CONCRETE-QUASIBRITTLE-MATERIALS-ZDEN.

[4] A. Hillerborg, M. Modéer, P.E. Petersson, Analysis of crack formation and crack growth in concrete by means of fracture mechanics and finite elements, Cem Concr Res. 6 (1976) 773–781. https://doi.org/10.1016/0008-8846(76)90007-7.

[5] Fracture Mechanics of Concrete Structures : Proceedings of the First International Conference on Fracture Mechanics of Concrete Structures (FraMCoS1), held at Beaver Run Resort,

Breckenridge, Colorado, USA, 1-5 June 1992., Fracture Mechanics of Concrete Structures. (2003). https://doi.org/10.1201/9781482286847.

[6] K.L. Scrivener, A.K. Crumbie, P. Laugesen, The Interfacial Transition Zone (ITZ) Between Cement Paste and Aggregate in Concrete, Interface Science 2004 12:4. 12 (2004) 411–421. https://doi.org/10.1023/B:INTS.0000042339.92990.4C.

[7] B.L. Karihaloo, Fracture Mechanics and Structural Concrete (Concrete Design and Construction Series), Ed. Longman Scientific & Technical. United States. (1995).

[8] S. Muralidhara, B.K.R. Prasad, H. Eskandari, B.L. Karihaloo, Fracture process zone size and true fracture energy of concrete using acoustic emission, Constr Build Mater. 24 (2010) 479–486. https://doi.org/10.1016/j.conbuildmat.2009.10.014.

[9] K. Otsuka, H. Date, Fracture process zone in concrete tension specimen, Eng Fract Mech. 65 (2000) 111–131. https://doi.org/10.1016/S0013-7944(99)00111-3.

[10] I. Kumpova, T. Fila, D. Vavrik, Z. Kersner, X-ray dynamic observation of the evolution of the fracture process zone in a quasi-brittle specimen, Journal of Instrumentation. 10 (2015) C08004. https://doi.org/10.1088/1748-0221/10/08/C08004.

[11] I. Kumpova, M. Vopalensky, T. Fila, D. Kytyr, D. Vavrik, M. Pichotka, J. Jakubek, Z. Kersner, J. Klon, S. Seitl, J. Sobek, On-the-Fly Fast X-Ray Tomography Using a CdTe Pixelated Detector - Application in Mechanical Testing, IEEE Trans Nucl Sci. 65 (2018) 2870–2876. https://doi.org/10.1109/TNS.2018.2873830.

[12] S. Brisard, M. Serdar, P.J.M. Monteiro, Multiscale X-ray tomography of cementitious materials: A review, Cem Concr Res. 128 (2020) 105824. https://doi.org/10.1016/J.CEMCONRES.2019.105824.

[13] L. Cedolin, S. Dei Poli, I. Iori, Experimental determination of the fracture process zone in concrete, Cem Concr Res. 13 (1983) 557–567. https://doi.org/10.1016/0008-8846(83)90015-7.

[14] L. Cedolin, S.D. Poli, I. Iori, Tensile Behavior of Concrete, J Eng Mech. 113 (1987) 431–449. https://doi.org/10.1061/(ASCE)0733-9399(1987)113:3(431).

[15] S. Bhowmik, S. Ray, An experimental approach for characterization of fracture process zone in concrete, Eng Fract Mech. 211 (2019) 401–419. https://doi.org/10.1016/J.ENGFRACMECH.2019.02.026.

[16] S. Das, M. Aguayo, G. Sant, B. Mobasher, N. Neithalath, Fracture process zone and tensile behavior of blended binders containing limestone powder, Cem Concr Res. 73 (2015) 51–62. https://doi.org/10.1016/j.cemconres.2015.03.002.

[17] S. Li, X. Fan, X. Chen, S. Liu, Y. Guo, Development of fracture process zone in full-graded dam concrete under three-point bending by DIC and acoustic emission, Eng Fract Mech. 230 (2020) 106972. https://doi.org/10.1016/J.ENGFRACMECH.2020.106972.

[18] Y. Guo, X. Chen, J. Liu, T. Chen, J. Wu, Effect of interface roughness on fracture energy and fracture process zone of rock-concrete specimens, Fatigue Fract Eng Mater Struct. 46 (2023) 574–589. https://doi.org/10.1111/FFE.13886.

[19] S. Miao, P.Z. Pan, W. Hou, B. He, P. Yu, Stress intensity factor evolution considering fracture process zone development of granite under monotonic and stepwise cyclic loading, Eng Fract Mech. 273 (2022) 108727. https://doi.org/10.1016/J.ENGFRACMECH.2022.108727.

[20] Y. Guo, X. Chen, Z. Wang, Y. Ning, L. Bai, Identification of mixed mode damage types on rock-concrete interface under cyclic loading, Int J Fatigue. 166 (2023) 107273. https://doi.org/10.1016/J.IJFATIGUE.2022.107273.

[21] S. Khalilpour, E. BaniAsad, M. Dehestani, A review on concrete fracture energy and effective parameters, Cem Concr Res. 120 (2019) 294–321. https://doi.org/10.1016/J.CEMCONRES.2019.03.013.

[22] H. Cifuentes, B.L. Karihaloo, Determination of size-independent specific fracture energy of normal- and high-strength self-compacting concrete from wedge splitting tests, Constr Build Mater. 48 (2013) 548–553. https://doi.org/https://doi.org/10.1016/j.conbuildmat.2013.07.062.

[23] N. Zhang, A. Hedayat, H.G. Bolaños Sosa, J. Tunnah, J.J. González Cárdenas, G.E. Salas Álvarez, Estimation of the mode I fracture toughness and evaluations on the strain behaviors of the compacted mine tailings from full-field displacement fields via digital image correlation, Theoretical and Applied Fracture Mechanics. 114 (2021) 103014. https://doi.org/10.1016/J.TAFMEC.2021.103014.

[24] N. Zhang, A. Hedayat, H.G. Bolaños Sosa, N. Tupa, I. Yanqui Morales, R.S. Canahua Loza, Mechanical and fracture behaviors of compacted gold mine tailings by semi-circular bending tests and digital image correlation, Constr Build Mater. 306 (2021) 124841. https://doi.org/10.1016/J.CONBUILDMAT.2021.124841.

[25] K.N. Rahal, M.P. Collins, Background to the general method of shear design in the 1994 CSA-A23.3 standard, Canadian Journal of Civil Engineering. 26 (1999) 827–839. https://www.proquest.com/scholarly-journals/background-general-method-shear-design-1994-csa/docview/213441503/se-2?accountid=17115.

[26] J. Lee, M. Nishiyama, S. Kono, M. Sakashita, Diagonal Tension Failure of Reinforced and Prestressed Concrete Member, ACI Struct J. 112 (2015) 311–321. https://www.proquest.com/scholarly-journals/diagonal-tension-failure-reinforced-prestressed/docview/1680122564/se-2?accountid=17115.

[27] F. Cavagnis, M. Fernández Ruiz, A. Muttoni, Shear failures in reinforced concrete members without transverse reinforcement: An analysis of the critical shear crack development on the basis of test results, Eng Struct. 103 (2015) 157–173. https://doi.org/10.1016/J.ENGSTRUCT.2015.09.015.

[28] T.N.H. Nguyen, K.H. Tan, T. Kanda, Investigations on web-shear behavior of deep precast, prestressed concrete hollow core slabs, Eng Struct. 183 (2019) 579–593. https://doi.org/10.1016/J.ENGSTRUCT.2018.12.052.

[29] E. Cuenca, P. Serna, Failure modes and shear design of prestressed hollow core slabs made of fiber-reinforced concrete, Compos B Eng. 45 (2013) 952–964. https://doi.org/10.1016/J.COMPOSITESB.2012.06.005.

[30] T. Karmokar, A. Mohyeddin, J. Lee, T. Paraskeva, Concrete cone failure of single cast-in anchors under tensile loading – A literature review, Eng Struct. 243 (2021) 112615. https://doi.org/10.1016/J.ENGSTRUCT.2021.112615.

[31] L.P. Pook, Five decades of crack path research, Eng Fract Mech. 77 (2010) 1619–1630. https://doi.org/10.1016/j.engfracmech.2010.04.010.

[32] L.P. Pook, Crack Paths, WIT Press, 2002. https://books.google.cz/books?id=PuJRAAAAMAAJ.

[33] J. Qian, A. Fatemi, Mixed mode fatigue crack growth: A literature survey, Eng Fract Mech. 55 (1996) 969–990. https://doi.org/10.1016/S0013-7944(96)00071-9.

[34] F. Erdogan, G.C. Sih, On the Crack Extension in Plates Under Plane Loading and Transverse Shear, Journal of Basic Engineering. 85 (1963) 519–525. https://doi.org/10.1115/1.3656897.

[35] G.C. Sih, Strain-energy-density factor applied to mixed mode crack problems, Int J Fract. 10 (1974) 305–321. https://doi.org/10.1007/BF00035493.

[36] G. Lesiuk, P. Kucharski, J.A.F.O. Correia, A.M.P. de Jesus, C. Rebelo, L. Simões da Silva, Mixed mode (I+II) fatigue crack growth in puddle iron, Eng Fract Mech. 185 (2017) 175–192. https://doi.org/10.1016/J.ENGFRACMECH.2017.05.002.

[37] A.L.L. Silva, A.M.P. de Jesus, J. Xavier, J.A.F.O. Correia, A.A. Fernandes, Combined analytical-numerical methodologies for the evaluation of mixed-mode (I + II) fatigue crack growth rates in structural steels, Eng Fract Mech. 185 (2017) 124–138. https://doi.org/10.1016/J.ENGFRACMECH.2017.04.016.

[38] Q. Lin, H. Yuan, L. Biolzi, J.F. Labuz, Opening and mixed mode fracture processes in a quasi-brittle material via digital imaging, Eng Fract Mech. 131 (2014) 176–193. https://doi.org/10.1016/J.ENGFRACMECH.2014.07.028.

[39] C. Li, VECTOR CTD CRITERION APPLIED TO MIXED MODE FATIGUE CRACK GROWTH, Fatigue Fract Eng Mater Struct. 12 (1989) 59–65. https://doi.org/10.1111/J.1460-2695.1989.TB00508.X.

[40] S. Pommier, P. Lopez-Crespo, P.Y. Decreuse, A multi-scale approach to condense the cyclic elastic-plastic behaviour of the crack tip region into an extended constitutive model, Fatigue Fract Eng Mater Struct. 32 (2009) 899–915. https://doi.org/10.1111/J.1460-2695.2009.01392.X.

[41] Q. Lin, S. Wang, P.Z. Pan, W.W. Ji, Y. Lu, Fracture initiation under pure shear revisited: Remarks on the mode II fracture in quasi-brittle materials, Theoretical and Applied Fracture Mechanics. 109 (2020) 102700. https://doi.org/10.1016/J.TAFMEC.2020.102700.

[42] W.W. Ji, P.Z. Pan, Q. Lin, X.T. Feng, M.P. Du, Do disk-type specimens generate a mode II fracture without confinement?, International Journal of Rock Mechanics and Mining Sciences. 87 (2016) 48–54. https://doi.org/10.1016/J.IJRMMS.2016.05.010.

[43] Q. Lin, W.W. Ji, P.Z. Pan, S. Wang, Y. Lu, Comments on the mode II fracture from disk-type specimens for rock-type materials, Eng Fract Mech. 211 (2019) 303–320. https://doi.org/10.1016/J.ENGFRACMECH.2019.02.024.

[44] M.L. Williams, On the Stress Distribution at the Base of a Stationary Crack, J Appl Mech. 24 (1957) 109–114. https://doi.org/10.1115/1.4011454.

[45] M. Moazzami, M.R. Ayatollahi, H.R. Chamani, M. Guagliano, L. Vergani, Determination of higher order stress terms in cracked Brazilian disc specimen under mode I loading using digital image correlation technique, Opt Laser Technol. 107 (2018) 344–352. https://doi.org/10.1016/J.OPTLASTEC.2018.06.010.

[46] P. Miarka, A.S. Cruces, S. Seitl, L. Malíková, P. Lopez-Crespo, Evaluation of the SIF and T-stress values of the Brazilian disc with a central notch by hybrid method, Int J Fatigue. 135 (2020). https://doi.org/10.1016/j.ijfatigue.2020.105562.

[47] M. Abshirini, N. Soltani, P. Marashizadeh, On the mode I fracture analysis of cracked Brazilian disc using a digital image correlation method, Opt Lasers Eng. 78 (2016) 99–105. https://doi.org/10.1016/J.OPTLASENG.2015.10.006.

[48] S. Miao, P.Z. Pan, W. Hou, M. Li, Z. Wu, Determination of mode I fracture toughness of rocks with field fitting and J-integral methods, Theoretical and Applied Fracture Mechanics. 118 (2022) 103263. https://doi.org/10.1016/J.TAFMEC.2022.103263.

[49] J. Lee, G.L. Fenves, Plastic-Damage Model for Cyclic Loading of Concrete Structures, J Eng Mech. 124 (1998) 892–900. https://doi.org/10.1061/(ASCE)0733-9399(1998)124:8(892).

[50] P. Grassl, D. Xenos, U. Nyström, R. Rempling, K. Gylltoft, CDPM2: A damage-plasticity approach to modelling the failure of concrete, Int J Solids Struct. 50 (2013) 3805–3816. https://doi.org/10.1016/J.IJSOLSTR.2013.07.008.

[51] F.C. Caner, Z.P. Bažant, Microplane Model M7 for Plain Concrete. I: Formulation, J Eng Mech. 139 (2013) 1714–1723. https://doi.org/10.1061/(ASCE)EM.1943-7889.0000570.

[52] J. Vorel, M. Marcon, G. Cusatis, F. Caner, G. di Luzio, R. Wan-Wendner, A comparison of the state of the art models for constitutive modelling of concrete, Comput Struct. 244 (2021) 106426. https://doi.org/10.1016/J.COMPSTRUC.2020.106426.

[53] L. Malíková, V. Veselý, The influence of higher order terms of Williams series on a more accurate description of stress fields around the crack tip, Fatigue Fract Eng Mater Struct. 38 (2015) 91–103. https://doi.org/10.1111/FFE.12221.

[54] R.J. Sanford, J.W. Dally, A general method for determining mixed-mode stress intensity factors from isochromatic fringe patterns, Eng Fract Mech. 11 (1979) 621–633. https://doi.org/10.1016/0013-7944(79)90123-1.

[55] T. Oplt, P. Hutar, P. Pokorný, L. Náhlík, Z. Chlup, F. Berto, Effect of the free surface on the fatigue crack front curvature at high stress asymmetry, Int J Fatigue. 118 (2019) 249–261. https://doi.org/10.1016/J.IJFATIGUE.2018.08.026.

[56] M.M. Mirsayar, Mixed mode fracture analysis using extended maximum tangential strain criterion, Mater Des. 86 (2015) 941–947. https://doi.org/10.1016/J.MATDES.2015.07.135.

[57] M.M. Mirsayar, A. Razmi, M.R.M. Aliha, F. Berto, EMTSN criterion for evaluating mixed mode I/II crack propagation in rock materials, Eng Fract Mech. 190 (2018) 186–197. https://doi.org/10.1016/J.ENGFRACMECH.2017.12.014.

[58] D.J. Smith, M.R. Ayatollahi, M.J. Pavier, The role of T-stress in brittle fracture for linear elastic materials under mixed-mode loading, Fatigue Fract Eng Mater Struct. 24 (2001) 137–150. https://doi.org/10.1046/J.1460-2695.2001.00377.X.

[59] M.R. Ayatollahi, M. Rashidi Moghaddam, F. Berto, T-stress effects on fatigue crack growth – Theory and experiment, Eng Fract Mech. 187 (2018) 103–114. https://doi.org/10.1016/J.ENGFRACMECH.2017.10.025.

[60] M.R. Ayatollahi, M.R.M. Aliha, On the use of Brazilian disc specimen for calculating mixed mode I–II fracture toughness of rock materials, Eng Fract Mech. 75 (2008) 4631–4641. https://doi.org/10.1016/J.ENGFRACMECH.2008.06.018.

[61] S. Seitl, P. Miarka, V. Bílek, The mixed-mode fracture resistance of C 50/60 and its suitability for use in precast elements as determined by the Brazilian disc test and three-point bending specimens, Theoretical and Applied Fracture Mechanics. 97 (2018). https://doi.org/10.1016/j.tafmec.2018.08.003.

[62] P. Miarka, S. Seitl, M. Horňáková, P. Lehner, P. Konečný, O. Sucharda, V. Bílek, Influence of chlorides on the fracture toughness and fracture resistance under the mixed mode I/II of high-performance concrete, Theoretical and Applied Fracture Mechanics. 110 (2020) 102812. https://doi.org/10.1016/J.TAFMEC.2020.102812.

[63] P. Miarka, S. Seitl, V. Bílek, Mixed-mode fracture analysis in high-performance concrete using a Brazilian disc test, Materiali in Tehnologije. 53 (2019). https://doi.org/10.17222/mit.2018.161.

[64] C. Hou, Z. Wang, W. Liang, J. Li, Z. Wang, Determination of fracture parameters in center cracked circular discs of concrete under diametral loading: A numerical analysis and experimental results, Theoretical and Applied Fracture Mechanics. 85 (2016) 355–366. https://doi.org/10.1016/J.TAFMEC.2016.04.006.

[65] F. Ouchterlony, Suggested methods for determining the fracture toughness of rock, in: International Journal of Rock Mechanics and Mining Sciences & Geomechanics Abstracts, 1988: pp. 71–96.

[66] H. Tada, P.C. Paris, G.R. Irwin, A.S. of M. Engineers., A.S.M. International., The stress analysis of cracks handbook, 3rd ed., ASME Press : Professional Engineering Pub. : ASM International, New York, 2000.

[67] T. Fett, Stress intensity factors and T-stress for internally cracked circular disks under various boundary conditions, Eng Fract Mech. 68 (2001) 1119–1136. https://doi.org/10.1016/S0013-7944(01)00025-X.

[68] P.S. Leevers, J.C. Radon, Inherent stress biaxiality in various fracture specimen geometries, International Journal of Fracture 1982 19:4. 19 (1982) 311–325. https://doi.org/10.1007/BF00012486.

[69] C.F. Shih, Small-Scale Yielding Analysis of, in: Proceedings of the 1973 National Symposium on Fracture Mechanics, University of Maryland, College Park, Md., 27-29 Aug. 1973, 1974: p. 187.

[70] V. Bilek, F. Khestl, P. Mec, Hybrid Cements with Non Silicate Activators, Solid State Phenomena. 259 (2017) 30–34. https://doi.org/10.4028/WWW.SCIENTIFIC.NET/SSP.259.30.

[71] Vic-2D V6 Reference Manual, Correlated Solutions Incorporated (C.S.Inc), (n.d.).

[72] H. Schreier, J.J. Orteu, M.A. Sutton, Image correlation for shape, motion and deformation measurements: Basic concepts, theory and applications, Image Correlation for Shape, Motion and Deformation Measurements: Basic Concepts,Theory and Applications. (2009) 1–321. https://doi.org/10.1007/978-0-387-78747-3.

[73] W.F. Clocksin, J.Q. da Fonseca, P.J. Withers, P.H.S. Torr, Image processing issues in digital strain mapping, in: A.G. Tescher (Ed.), Proceedings of SPIE, Application of Digital Image Processing XXV, 2002: pp. 384–395.

[74] M. Mokhtarishirazabad, P. Lopez-Crespo, B. Moreno, A. Lopez-Moreno, M. Zanganeh, Optical and analytical investigation of overloads in biaxial fatigue cracks, Int J Fatigue. 100 (2017) 583–590. https://doi.org/10.1016/J.IJFATIGUE.2016.12.035.

[75] P. López-Crespo, R.L. Burguete, E.A. Patterson, A. Shterenlikht, P.J. Withers, J.R. Yates, Study of a crack at a fastener hole by digital image correlation, Exp Mech. 49 (2009) 551–559. https://doi.org/10.1007/S11340-008-9161-1/FIGURES/8.

[76] Matlab, version 9.10.0 (R2018a), The MathWorks Inc., 2018.

[77] P. Lopez-Crespo, A. Shterenlikht, J.R. Yates, E.A. Patterson, P.J. Withers, Some experimental observations on crack closure and crack-tip plasticity, Fatigue Fract Eng Mater Struct. 32 (2009) 418–429. https://doi.org/10.1111/J.1460-2695.2009.01345.X.

[78] P. Lopez-Crespo, A. Shterenlikht, E.A. Patterson, J.R. Yates, P.J. Withers, The stress intensity of mixed mode cracks determined by digital image correlation:, Journal of Strain Analysis for Engineering Design. 43 (2008) 769–780. https://doi.org/10.1243/03093247JSA419.

[79] M. Zanganeh, P. Lopez-Crespo, Y.H. Tai, J.R. Yates, Locating the Crack Tip Using Displacement Field Data: A Comparative Study, Strain. 49 (2013) 102–115. https://doi.org/10.1111/STR.12017.

[80] L. Chen, G. Zhang, Z. Zou, Y. Guo, X. Zheng, The effect of fracture growth rate on fracture process zone development in quasi-brittle rock, Eng Fract Mech. 258 (2021) 108086. https://doi.org/10.1016/J.ENGFRACMECH.2021.108086.

[81] Y. Jianhong, F.Q. Wu, J.Z. Sun, Estimation of the tensile elastic modulus using Brazilian disc by applying diametrically opposed concentrated loads, International Journal of Rock Mechanics and Mining Sciences. 46 (2009) 568–576. https://doi.org/10.1016/J.IJRMMS.2008.08.004.

[82] L. Malíková, Multi-parameter fracture criteria for the estimation of crack propagation direction applied to a mixed-mode geometry, Eng Fract Mech. 143 (2015) 32–46. https://doi.org/10.1016/J.ENGFRACMECH.2015.06.029.

[83] G.R. Irwin, Plastic Zone Near a Crack and Fracture Toughness., in: Sagamore Research Conference, 1961: pp. 63–78.

[84] M.R. Ayatollahi, J. Akbardoost, Size effects on fracture toughness of quasi-brittle materials – A new approach, Eng Fract Mech. 92 (2012) 89–100. https://doi.org/10.1016/J.ENGFRACMECH.2012.06.005.

[85] K. Otsuka, H. Date, Fracture process zone in concrete tension specimen, Eng Fract Mech. 65 (2000) 111–131. https://doi.org/10.1016/S0013-7944(99)00111-3.

[86] Z.P. Bazant, Mechanics of fracture and progressive cracking in concrete structures, Fract Mech of Concr, Struct Appl and Numer Calc. (1985) 1–94. https://doi.org/10.1007/978-94-009-6152-4_1.

[87] N. Alanazi, L. Susmel, Theory of Critical Distances and static/dynamic fracture behaviour of un-reinforced concrete: length scale parameters vs. material meso-structural features, Eng Fract Mech. 261 (2022) 108220. https://doi.org/10.1016/J.ENGFRACMECH.2021.108220.

[88] Determination of the fracture energy of mortar and concrete by means of three-point bend tests on notched beams, Materials and Structures 1985 18:4. 18 (1985) 287–290. https://doi.org/10.1007/BF02472918.

[89] P. Miarka, S. Seitl, W. de Corte, Notch tip displacements of the concrete Brazilian disc test with central notch analysed by the concrete damaged plasticity model, Theoretical and Applied Fracture Mechanics. 102 (2019). https://doi.org/10.1016/j.tafmec.2019.04.006.

[90] A. Aminzadeh, B. Bahrami, M.R. Ayatollahi, M. Nejati, On the role of fracture process zone size in specifying fracturing mechanism under dominant mode II loading, Theoretical and Applied Fracture Mechanics. 117 (2022) 103150. https://doi.org/10.1016/J.TAFMEC.2021.103150.

[91] Z.P. Bazant, M. Hasegawa, J. Mazars, Size Effect in Brazilian Split-Cylinder Tests: Measurements and Fracture Analysis, Materials Journal. 88 (1991) 325–332. https://doi.org/10.14359/1987.